Earth, Planets and Space

FULL PAPER Open Access

Evaluation of candidate models for the 14th generation International Geomagnetic Reference Field

C. D. Beggan[1*], C. Kloss[2], A. Grayver[3], P. Alken[4,5], G. Balasis[6], W. Brown[1], S. Califf[4,5], L. Chauvet[7], A. Chulliat[4,5], M. Fillion[7], L. Gailler[8], G. Hulot[7], M. Korte[9], V. Lesur[7], Y. Lin[10], M. Matsushima[11], H. McCreadie, T. Minami[12], M. Nair[4,5], S. Nakano[13], F. J. Pavón-Carrasco[14,15], M. Rother[9], S. Sato[16], M. Serrano[14,15], M. V. da Silva[9], A. Smith[17], F. Terra-Nova[18], E. Thebault[8], H. Toh[16], I. Wardinski[19] and C. Xiong[20]

Abstract

In November 2024, the 14th revision of the International Geomagnetic Reference Field (IGRF) was issued by the International Association of Geomagnetism and Aeronomy (IAGA) Division V Working Group (V-MOD). This revision comprises two new spherical harmonic main field models for epochs 2020.0 (DGRF-2020) and 2025.0 (IGRF-2025) and a model of the predicted secular variation for the interval 2025.0—2030.0 (SV-2025–2030), all provided as internal Gauss coefficients to degree and order 13 for DGRF-2020 and IGRF-2025, and degree and order 8 for SV-2025–2030. The models were produced from candidates submitted by nineteen international teams. The candidate models were evaluated by an expert international volunteer Taskforce. Comparisons between all candidates as well as to mean, median and Huber-weighted averages of all candidates were made using well-established statistical criteria. These analyses were used to identify, for example, the variation between Gauss coefficients or geographical regions, where the candidate models strongly differed. The majority of candidates were sufficiently close that the differences can be explained primarily by individual modelling methodologies and data selection strategies. None of the candidates were sufficiently different to warrant their exclusion. The IAGA V-MOD Taskforce thus voted for two approaches: the median of the Gauss coefficients of the candidates for the DGRF-2020 and the computed Huber mean in space for the IGRF-2025 and SV-2025–2030 models. In this paper, we document the evaluation of the candidate models and provide details of the approach used to derive the final IGRF-14 products.

Keywords IGRF, Magnetic field modelling, Geomagnetism

*Correspondence:
C. D. Beggan
ciar@bgs.ac.uk
Full list of author information is available at the end of the article

Graphical Abstract

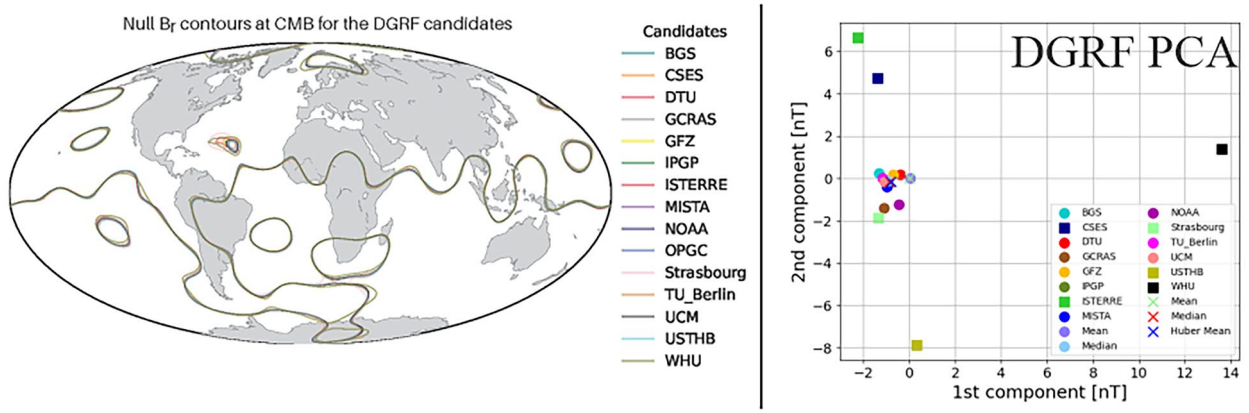

1 Introduction

The International Geomagnetic Reference Field (IGRF) is a series of mathematical models describing the large-scale internal source of Earth's magnetic field. The models are a set of spherical harmonic coefficients. Models are submitted by a community of researchers with the final set of coefficients agreed upon by an international task force of geomagnetic field modelling experts (Beggan et al. 2026). The models are updated every 5 years to account for the time variations of the field originating in Earth's core to reduce errors to below the measurement uncertainty of the average user (e.g. Beggan 2022).

The IGRF model is used by academia, government, and industry in a wide variety of studies, including magnetic reference systems, long-term dynamics of the Earth's core field, ionospheric electrodynamics, space weather phenomena, electromagnetic induction, local magnetic anomalies in the Earth's crust, and surveying. It is also used for orientation in three dimensions, for example, in satellite attitude determination or augmented/virtual reality devices. Readers interested in the history of IGRF are referred to Barton (1997) and Macmillan and Finlay (2011). The purpose of this paper is to summarize the candidate models which were submitted for consideration for the fourteenth generation of International Geomagnetic Reference Field (hereafter IGRF-14) and to report the methods used by the Taskforce to evaluate the candidates and construct the final IGRF-14 models.

1.1 Taskforce remit

The volunteer IGRF Taskforce, consisting of the authors of this study, operates under the auspices of the International Association of Geomagnetism and Aeronomy (IAGA) Division V Working Group on Modelling (also known as V-MOD). The IGRF-14 Taskforce chairs (Beggan and Kloss) were formally elected at an IAGA V-MOD Business Meeting in Berlin in July 2023, and a general call for additional members was issued in January 2024. On 13 March 2024, the Taskforce issued an international call (via professional email lists) for modelling teams to contribute candidates for: (1) a new definitive geomagnetic reference field (DGRF) for epoch 2020.0 to spherical harmonic (SH) degree and order 13, (2) a new provisional IGRF for epoch 2025.0 to SH degree and order 13, and (3) a predictive linear secular variation (SV) forecast for the interval 2025.0 to 2030.0 to SH degree and order 8. The term 'definitive' is used, because the best available data sets before and after the epoch were used by the modelling teams, and any further substantial improvement of these retrospectively determined models is unlikely. In contrast, the 'provisional' IGRF for epoch 2025.0 will eventually be replaced by a definitive model in a future revision of the IGRF when the community has more complete measurements of the Earth's magnetic field for epoch 2025.0.

1.2 Candidate teams

In total, nineteen international teams participated in the IGRF-14 call. Fourteen (14) candidate models were received for the 2020 DGRF, fifteen (15) for the 2025 IGRF, and eighteen (18) for the 2025–2030 SV forecast. The nineteen teams who participated in the IGRF-14 call were led by the British Geological Survey (UK), National Institute of Natural Hazards (China), Technical University of Denmark (Denmark), University of Edinburgh (UK), GFZ Helmholtz–Zentrum für Geoforschung

Table 1 Teams submitting IGRF-14 candidate models. Additional documentation is available in Beggan et al. (2024)

Lead Institute (Team Abbreviation)	Country/Region	DGRF	IGRF	SV	Paper Reference
British Geological Survey (BGS)	UK	✓	✓	✓	-
National Institute of Natural Hazards, China Seismo-Electromagnetic Satellite (CSES)	China	✓	✓	✓	Yang et al. (2026)
DTU Space (DTU)	Denmark	✓	✓	✓	Kloss et al. (2026)
University of Edinburgh (Edinburgh)	UK	-	-	✓	Madsen et al. (2026)
GFZ Helmholtz–Zentrum für Geoforschung (GFZ)	Germany	✓	✓	✓	Rother et al. (2026)
Geophysical Center of the Russian Academy of Sciences (GC RAS)	Russia	✓	✓	-	Firsov et al. (2026)
Université Paris Cité, Institut de physique du globe de Paris (IPGP)	France	✓	✓	✓	Hulot et al. (2026)
Institute of Earth Science (IS Terre)	France	✓	✓	✓	Claveau et al. (2025)
University of Kyoto (Japan)	Japan	-	-	✓	Sato et al. (2026)
University of Leeds (Leeds)	UK	-	-	✓	Shakespeare-Rees et al. (2026)
Macau Institute of Space Technology and Application (MISTA)	Macau	✓	✓	✓	Yao et al. (2025)
NASA Goddard Space Flight Centre (NASA)	USA	-	-	✓	Gwirtz et al. (2025)
University of Colorado/National Centers for Environmental Information, NOAA (NOAA)	USA	✓	✓	✓	Chulliat et al. (2026)
Observatoire de Physique du Globe de Clermont–Ferrand (OPGC/LMV)	France	-	✓	✓	-
University of Strasbourg (Strasbourg)	France	✓	✓	✓	Wardinski et al. (2026)
Technical University of Berlin (TU Berlin)	Germany	✓	✓	✓	-
Universidad Complutense de Madrid (UCM)	Spain	✓	✓	✓	Serrano et al. (2026)
University of Science and Technology – Houari Boumediene (USTHB)	Algeria	✓	✓	✓	-
Wuhan University (WHU)	China	✓	✓	✓	Qian et al. (2025)

(Germany), Geophysical Center of the Russian Academy of Sciences (Russia), Institut de physique du globe de Paris (France), Institut des Sciences de la Terre (France), Kyoto University (Japan), University of Leeds (UK), Macau Institute of Space Technology and Application (China), NASA Goddard Space Flight Center (USA), University of Colorado Boulder/National Centers for Environmental Information, NOAA (USA), Observatoire de Physique du Globe de Clermont–Ferrand (France), Université de Strasbourg (France), Technical University of Berlin (Germany), Universidad Complutense de Madrid (Spain), University of Science and Technology Houari Boumediene (Algeria) and Wuhan University (China), see Table 1 for a summary of the models submitted by each team as well as references describing the preparation of each candidate model in detail.

The number of institutions participating in IGRF-14 is larger than any previous generation, highlighting the advance of global capability in this area of research. The drivers for this increase include the launch of several new satellite missions such as the Macau Science Satellite 1 (MSS-1) in 2023 and the continued widespread availability of high quality data from the European Space Agency (ESA) Swarm mission, as well as contributions from institutes which operate high quality ground-based observatories. The knowledge and capability to produce main field models has also grown along with the diminishing cost and access to high-performance computing. The composition of the teams shows strong cooperation between scientists both within their own countries and internationally.

The candidate models were primarily built using data from the ESA Swarm constellation (2013–present) (Friis-Christensen et al. 2006), including experimental vector data from its Absolute Scalar Magnetometer (ASM) instrument (Léger et al. 2015; Hulot et al. 2015), and the MSS-1 mission (Zhang 2023). The launch of the China Earthquake Administration China Seismo-Electromagnetic Satellite (CSES) mission (Shen et al. 2018) in 2019 provides a new source of global magnetic field data, which was utilized by Yang et al. (2026), for example. In addition, ground observatories play a vital role in ensuring the continuous coverage of the temporal variation of the magnetic field at over 150 locations on the Earth's surface, many under the umbrella of INTERMAGNET, a voluntary network of observatories who aim to provide high quality near-real-time data (e.g. Brown et al. 2025; Love and Chulliat 2013). Table 4 in Beggan et al. (2026) lists the institutes contributing geomagnetic observatory data. Satellite and ground observatory data complement each other and both are essential for high quality magnetic field modelling.

1.3 Modelling synopsis

We briefly summarize the data selection, processing, and modelling procedures used. A novel development in IGRF-14 is the use of machine learning for secular variation forecasting (Sato et al. 2026; Shakespeare-Rees et al. 2026). The detailed descriptions of the techniques used to derive the individual candidate models can be found in the papers appearing in this special issue (see Table 1). Note that most teams have also provided additional background documentation in the IAGA V-MOD IGRF-14 Evaluation GitHub repository (Beggan et al. 2024).

For the main field candidates at 2020.0 and 2025.0, some teams derived their candidate models from parent models describing the magnetic field over periods longer than requested by IGRF (e.g. Claveau et al. 2025; Wardinski et al. 2026; Hulot et al. 2026). Such models typically involve internal temporal parameterization using splines and external field parameterization of varying complexity. Other teams focused their effort on dedicated internal candidate models for each of the epochs, using data within windows centered on 2020, or immediately preceding 2025 (e.g. Chulliat et al. 2026; Firsov et al. 2026; Serrano et al. 2026) which requires less complex parameterization in space and in time but different data selection and pre-processing to minimize magnetic field contributions, such as external fields. In general, all candidate models rely on some geographical and/or iterative statistical weighting schemes to down-weight measurements more contaminated by external field sources (e.g., the auroral zones). New techniques to better capture the magnetic field in the auroral zones were applied by Kloss et al. (2026).

One of the remaining unsolved challenges in geomagnetism is the accurate prediction of the magnetic field change over the 5-year epochs (Hulot et al. 2010). Despite decades of research, the average accuracy remains around 20 nT/year root-mean-square (RMS) in forecasting the temporal evolution of the main geomagnetic field (e.g. Alken et al. 2021b). This inadequacy relates to the low resolution of the recoverable magnetic field at the core–mantle boundary, the occurrence of unpredictable geomagnetic jerks (Gillet et al. 2024) and the uncertainty associated with diffusion of the field over short timescales (Metman et al. 2019). It is also noteworthy that the northern polar regions have experienced unusually large variations in the past three decades compared to the southern hemisphere (Livermore et al. 2017).

For forecasting SV, the teams used computational, physics-based or machine learning approaches such as assimilation of magnetic field measurements into a geodynamo model (Gwirtz et al. 2025) or setting up a localized model of flow using a neural net (Shakespeare-Rees et al. 2026) to improve the forecast. Other teams used mathematical extrapolation of the Gauss coefficients over shorter or longer periods, assuming that the magnetic field will behave in a similar manner to the previous few years (Qian et al. 2025; Yao et al. 2025; Serrano et al. 2026). Others opted to enforce periodic behavior on the flow coefficients to estimate SV (Madsen et al. 2026; Sato et al. 2026).

1.4 Final model synthesis

The volunteers of the IGRF-14 Taskforce carried out evaluations of the candidate models submitted by the teams. Assessment of the candidate models was primarily based on statistical criteria. However, a good statistical agreement between models does not necessarily mean that these models are an accurate representation of the true field. It can also be a consequence of methodological biases common to all or to a majority of them. For this reason, the candidate model evaluation also relied on companion descriptions of the candidate models as well as on their expert opinion and comparisons with semi-independent data sets, such as appropriately processed satellite or observatory data.

During the autumn of 2024, the Taskforce evaluated each candidate model using both well-established methodologies and novel approaches. To decide the mechanism for deriving the final models, the members were balloted and the accepted IGRF-14 models were established by a vote on the different recommendations submitted by the Taskforce. The vote was held in early November 2024. The Taskforce chose to select the median of all candidate model coefficients in each degree and order for the DGRF-2020 model. An iterative robust weighting in space for the IGRF-2025 main field and SV-2025–2030 models was chosen. The final model coefficients can be recreated using the candidate models and code provided in Beggan et al. (2024).

The IGRF-14 was formally released on 22 November 2024. The resulting Gauss coefficients were prepared and checked before being made available to the public through the IAGA Division V-MOD working group web page (http://www.ngdc.noaa.gov/IAGA/vmod/igrf.html). Example code and check values were also made available as part of the IGRF outputs. Updated web services and online calculators are also available for public use. The official set of spherical harmonic coefficients and all the IGRF-14 candidate models can be found in the dedicated IAGA V-MOD GitHub repository. In addition, the Gauss coefficients in various text formats were placed into a Zenodo repository (International Association of Geomagnetism and Aeronomy 2024).

The remainder of this paper describes the methods and statistical criteria used by the Taskforce to test and compare the candidate models, and explains how the final versions released in November 2024 were derived.

2 Methodology

We follow a standard and well-established methodology for evaluation of main field models by comparing them spectrally and spatially for similarities and differences to find obvious disagreements (e.g. Finlay et al. 2010; Thébault et al. 2015; Alken et al. 2021a). Assuming there are no local magnetic field sources in the IGRF region of validity, the global magnetic field can be expressed as the gradient of a scalar potential, $\mathbf{B} = -\nabla V$. Though the assumption of a source-free region is not strictly true (e.g. due to the ionospheric current systems, lightning in the atmosphere or field-aligned currents in space), the scalar potential V may be approximated as a finite series:

$$V(r,\theta,\phi,t) = a\sum_{n=1}^{N}\sum_{m=0}^{n}\left(\frac{a}{r}\right)^{n+1} \left[g_n^m(t)\cos(m\phi) + h_n^m(t)\sin(m\phi)\right]P_n^m(\cos\theta) \quad (1)$$

Here, $g_n^m(t)$ and $h_n^m(t)$ are the Gauss coefficients which depend on time t, conventionally given in units of nanotesla (nT). The coordinates (r,θ,ϕ) are geocentric radius, co-latitude, and longitude, and $a = 6371.2$ km is the conventional value used in geomagnetism for the mean spherical Earth radius (Winch et al. 2005). The functions P_n^m are the Schmidt quasi-normalized associated Legendre functions of degree n and order m. N specifies the spherical harmonic degree truncation value, which was chosen to be $N = 10$ up to and including epoch 1995. Starting from IGRF-9 (Macmillan et al. 2003), however, it was decided to increase N to N =13 thanks to the availability of high-quality satellite geomagnetic data providing enhanced geographic coverage. All subsequent IGRF releases have since kept with this use for all DGRF and IGRF models starting from epoch 2000.

In the evaluation of the candidate models, we compare them by computing differences of the Gauss coefficients and plotting spatial map differences. We also compared individual candidates with Gauss coefficients computed from the mean and median of all candidates. In addition, we calculated an estimate of the maximum likelihood model computed in space from all candidate models using a spatially based robust Huber iterative weighting scheme (known as the 'Huber' model). To build the Huber model, the Gauss coefficients of each candidate model were used to compute the vector geomagnetic field at the Earth's mean radius on an equal area grid with 10,000 nodes (Leopardi 2006). On each node, we have as many vector field values as candidate models. The variations among candidates at each node produce an ensemble of magnetic field values. The Huber algorithm in space iteratively reweights the magnetic values of each candidate on the grid according to its deviation from the ensemble of available candidate model vector field predictions. This produces Huber weights for each candidate model at each node for the three vector field components. The weights of values range from 0 to 1, illustrating regions where the candidate models agree (or disagree) with the ensemble of magnetic field predictions. This numerical computation is based on the Huber error distribution:

$$H(\epsilon) = \frac{1}{N_c}\begin{cases} \exp(-\epsilon^2/2), & |\epsilon| < c \\ \exp(-c|\epsilon| + c/2), & |\epsilon| \geq c \end{cases} \quad (2)$$

where N_c is the normalization factor that ensures the distribution integrates to unity. For each candidate model and at each node, the parameter ϵ is the normalized departure of the model prediction from that of the best estimation model and the constant c is chosen as a compromise between a Laplace distribution (obtained when $c = 0$) and a Gaussian distribution (obtained when $c \to \infty$). Our Huber weighting scheme uses $c = 1.345$ (Huber 1964; Olsen 2002).

All vector field values on the nodes of the grid are thus associated with their Huber weights. The final model is the inversion of the Huber-weighted spatial magnetic values from each candidate for the maximum likelihood average model in spherical harmonics (Thébault et al. 2015). The advantage of this method is that all candidates can contribute; if a candidate disagrees in some regions, while still agreeing in other regions, it can still provide an appropriate weighted input to the final model coefficients.

The Gauss coefficients of the Median, Mean and Huber models are provided on the IAGA Division V-MOD GitHub repository. We briefly define the mathematical expressions which were used to evaluate the IGRF-14 candidate models. Given their versatility, these are very similar to analyses used for the IGRF-11, IGRF-12 and IGRF-13 evaluations (Finlay et al. 2010; Thébault et al. 2015; Alken et al. 2021b) .

2.1 Model differences

The initial and simplest evaluation is of differences between two models to identify regions of strong discrepancies, both in the spatial and spectral domains. As the Gauss coefficients in the scalar potential (Eq. (1)) appear as linear terms, we can compute the direct differences of these parameters from two different models, and substitute the differences into the relevant equations, both for the scalar potential V and vector geomagnetic

field **B**. If we define the Gauss coefficients of a particular candidate model i by ${}_ig_n^m$ and ${}_ih_n^m$, then the coefficient difference between two models i and j is defined as

$$\begin{aligned} {}_{i,j}g_n^m &= {}_ig_n^m - {}_jg_n^m \\ {}_{i,j}h_n^m &= {}_ih_n^m - {}_jh_n^m \end{aligned} \tag{3}$$

These can be plotted as line graphs or triangle plots showing the degree and order differences.

2.2 Spherical harmonic power spectral differences

The mean square value of the vector geomagnetic field over a sphere of radius r due to all harmonics of SH degree n for a given candidate model i is

$${}_iR_n(r) = (n+1)\left(\frac{a}{r}\right)^{2n+4}\sum_{m=0}^{N}\left[({}_ig_n^m)^2 + ({}_ih_n^m)^2\right] \tag{4}$$

This is known as the Lowes–Mauersberger power spectrum (Lowes 1974; Mauersberger 1956), and may also be applied to the differences between two models,

$${}_{i,j}R_n(r) = (n+1)\left(\frac{a}{r}\right)^{2n+4}\sum_{m=0}^{N}\left[({}_{i,j}g_n^m)^2 + ({}_{i,j}h_n^m)^2\right] \tag{5}$$

Summing the power ${}_{i,j}R_n(r)$ over all SH degrees from 1 to the truncation level N and then taking the square root provides the root mean square (RMS) vector field difference between models i and j,

$${}_{i,j}R(r) = \sqrt{\sum_{n=1}^{N}{}_{i,j}R_n(r)} \tag{6}$$

2.3 Azimuthal power spectral differences

The Lowes–Mauersberger equation computes spectral power in terms of spherical harmonic degree n. It is also useful to analyze power as a function of the azimuthal ratio $az = m/n$, which varies from 0 for zonal harmonics to 1 for sectorial harmonics. We conventionally define the az ratio as positive for the g_n^m coefficients and negative for the h_n^m. The azimuthal power is then defined as the mean square value of the field over a sphere of radius r produced by all harmonics with the same azimuthal ratio. For model i, the azimuthal power spectrum is defined as

$${}_iR_{az}(r) = \sum_{(m,n)\in A_{az}}(n+1)\left(\frac{a}{r}\right)^{2n+4}\left[({}_ig_n^m)^2 + ({}_ih_n^m)^2\right] \tag{7}$$

where $A_{az} = \{(m,n) \in \mathbb{Z}\times\mathbb{Z} : m/n = az\}$. Note this analysis of the candidate models is provided in Beggan et al. (2024), though not shown here for the sake of brevity.

2.4 Degree correlation

The correlation per degree between two models i and j is defined as (Langel and Hinze 1998, pg. 81):

$${}_{i,j}\rho_n = \frac{\sum_{m=0}^{n}\left({}_ig_n^m{}_jg_n^m + {}_ih_n^m{}_jh_n^m\right)}{\sqrt{\left(\sum_{m=0}^{n}\left[({}_ig_n^m)^2 + ({}_ih_n^m)^2\right]\right)\left(\sum_{m=0}^{n}\left[({}_jg_n^m)^2 + ({}_jh_n^m)^2\right]\right)}} \tag{8}$$

Note that contrary to the spectral differences provided by Eqs. 5-7, this degree correlation does not depend on the choice of the variable r. To compute such degree correlations between a candidate model i and a reference model (such as the mean or median of all candidates) the ${}_jg_n^m, {}_jh_n^m$ coefficients just need to be replaced with the Gauss coefficients of the reference model in Eq. (8). This can provide guidance on whether the harmonics of a particular degree of the candidate may be substantially different if they correlate poorly with the reference model.

3 Evaluation of candidate models

To adhere to the principles of Findable, Accessible, Interoperable and Reusable (FAIR) science, the majority of the analysis and figures were generated using the open source Python code and IGRF-14 candidates available in the IAGA V-MOD IGRF14 Evaluation GitHub repository. Further plots and analysis for all candidates can be found in the repository of Beggan et al. (2024), where they can be freely inspected, reproduced and reused as desired.

3.1 Analysis of DGRF-2020 candidate models

The call for the DGRF-2020 requested models describing the large-scale internal field up to SH degree 13 with Gauss coefficients defined to a precision of 0.01 nT. We list the fourteen candidate models (and the respective references) received for epoch 2020.0 in Table 1. The majority of candidates used Swarm data in combination with ground observatories, though the Strasbourg team used exclusively ground observatory data to derive their model (Wardinski et al. 2026).

In Table 2, we present the root-mean-square (RMS) vector field differences (${}_{i,j}R$ in nT) between the individual candidate models i and j at the Earth's reference radius $r = a$. The last three columns show the RMS difference between each candidate model i and (a) the simple arithmetic Mean model, (b) the Median model and (c) the Huber-weighted model. The required precision of 0.01 nT leads to an estimate of the formal error due to truncation at $n = 13$ of 0.056 nT (Finlay et al. 2010; Lowes 2000).

Table 2 Root-mean-square vector field differences ${}_{i,j}R(r)$ at reference radius $r = a$ in units of nT between the various DGRF-2020 candidate models and between the candidate models and the Mean, Median and Huber DGRF-2020 models (three rightmost columns). The Avg Diff row is the simple arithmetic means ${}_{i}R$ of the ${}_{i,j}R$, where this includes all candidates

${}_{i,j}R$/nT	BGS	CSES	DTU	GCRAS	GFZ	IPGP	ISTerre	MISTA	NOAA	Strasbourg	TU Berlin	UCM	USTHB	WHU	Mean	Median	Huber
BGS	0	10.73	5.04	5.46	2.76	1.90	7.67	2.33	2.83	9.34	1.65	1.79	9.61	15.05	2.38	1.68	1.53
CSES	10.73	0	10.13	13.57	10.52	10.89	12.54	10.98	11.12	13.98	10.89	10.63	14.17	17.82	9.96	10.65	10.44
DTU	5.04	10.13	0	8.94	3.54	4.45	9.22	4.41	5.35	9.91	4.55	4.27	9.28	14.67	4.01	4.17	4.1
GCRAS	5.46	13.57	8.94	0	6.7	5.95	10.54	6.28	6.02	11.02	5.69	6.07	10.8	15.98	6.2	6.01	5.88
GFZ	2.76	10.52	3.54	6.7	0	2.92	8.24	3.08	3.94	9.32	2.19	2.85	9.34	14.58	2.53	2.53	2.24
IPGP	1.90	10.89	4.45	5.95	2.92	0	8.1	0.85	2.61	8.72	2.47	0.87	8.88	14.69	1.88	0.79	1.1
ISTerre	7.67	12.54	9.22	10.54	8.24	8.1	0	8.05	9.19	11.82	8.1	7.92	16.15	17.08	8.14	7.85	7.99
MISTA	2.33	10.98	4.41	6.28	3.08	0.85	8.05	0	2.77	8.61	2.91	1.17	8.88	14.76	2.09	1.05	1.46
NOAA	2.83	11.12	5.35	6.02	3.94	2.61	9.19	2.77	0	9.06	3.36	2.55	8.07	14.45	2.64	2.45	2.4
Strasbourg	9.34	13.98	9.91	11.02	9.32	8.72	11.82	8.61	9.06	0	9.47	8.88	11.67	17.07	8.32	8.67	8.69
TU Berlin	1.65	10.89	4.55	5.69	2.19	2.47	8.1	2.91	3.36	9.47	0	2.28	9.44	14.99	2.56	2.15	1.81
UCM	1.79	10.63	4.27	6.07	2.85	0.87	7.92	1.17	2.55	8.88	2.28	0	8.95	14.79	1.82	0.75	0.96
USTHB	9.61	14.17	9.28	10.8	9.34	8.88	16.15	8.88	8.07	11.67	9.44	8.95	0	16.71	8.72	8.93	8.84
WHU	15.05	17.82	14.67	15.98	14.58	14.69	17.08	14.76	14.45	17.07	14.99	14.79	16.71	0	13.61	14.62	14.48
Avg Diff	5.44	11.28	6.70	8.07	5.71	5.24	9.62	5.36	5.81	9.92	5.57	5.22	10.14	14.47	5.35	5.16	5.14

Table 3 Root-mean-square vector field differences ${}_{i,j}R(r)$ at reference radius $r = a$ in units of nT between the various IGRF-2025 candidate models and between the candidate models and the Mean, Median and Huber IGRF-2025 models (final three columns). The Avg Diff row is the simple arithmetic means ${}_{i}R$ of the ${}_{i,j}R$, where this includes all candidate models

${}_{i,j}R$/nT	BGS	CSES	DTU	GCRAS	GFZ	IPGP	ISTerre	MISTA	NOAA
BGS	0	15.07	6.62	9.91	12.35	8.06	9.3	7.27	4.8
CSES	15.07	0	14.06	18.1	12.73	15.62	14.97	15	14.45
DTU Space	6.62	14.06	0	10.8	8.59	8.06	12.51	3.49	7.21
GCRAS	9.91	18.1	10.8	0	13.8	14.04	14.14	10.97	10.66
GFZ	12.35	12.73	8.59	13.8	0	11.36	15.97	8.67	11.73
IPGP	8.06	15.62	8.06	14.04	11.36	0	11.19	8.47	8.34
ISTerre	9.3	14.97	12.51	14.14	15.97	11.19	0	12.8	10.05
MISTA	7.27	15	3.49	10.97	8.67	8.47	12.8	0	8.03
NOAA	4.8	14.45	7.21	10.66	11.73	8.34	10.05	8.03	0
OPGC/LMV	8.12	14.54	6.65	13.48	9.55	7.23	11.59	5.62	7.92
Strasbourg	53.58	52.75	52.8	56.17	53.59	53.27	54.38	53.38	53.29
TU Berlin	6.05	13.58	3.75	10.48	8.33	7.41	11.72	4.97	6.53
UCM	8.41	12.13	5.59	11.77	7.26	8.24	11.5	6.09	7.78
USTHB	14.31	20.51	11.53	18.11	15.83	15.26	20.29	11.4	15.32
WHU	20.76	23.22	22	26.81	23.83	20.09	21.23	22.97	21.26
Avg Diff	12.31	17.12	11.58	15.95	14.24	13.11	15.44	11.94	12.49
	OPGC/LMV	**Strasbourg**	**TU Berlin**	**UCM**	**USTHB**	**WHU**	**Mean**	**Median**	**Huber**
BGS	8.12	53.58	6.05	8.41	14.31	20.76	6.29	5.23	4.97
CSES	14.54	52.75	13.58	12.13	20.51	23.22	12.29	12.85	12.69
DTU Space	6.65	52.8	3.75	5.59	11.53	22	5.02	3.36	3.62
GCRAS	13.48	56.17	10.48	11.77	18.11	26.81	12	10.45	10.58
GFZ	9.55	53.59	8.33	7.26	15.83	23.83	9.11	8.49	8.38
IPGP	7.23	53.27	7.41	8.24	15.26	20.09	7.21	6.48	6.48
ISTerre	11.59	54.38	11.72	11.5	20.29	21.23	10.65	10.39	10.13
MISTA	5.62	53.38	4.97	6.09	11.4	22.97	6.07	4.21	4.4
NOAA	7.92	53.29	6.53	7.78	15.32	21.26	6.47	5.72	5.27
OPGC/LMV	0	53.18	6.57	6.68	13.74	22.36	6.57	5.38	5.23
Strasbourg	53.18	0	53.04	53.8	53.32	58.16	49.59	52.99	52.59
TU Berlin	6.57	53.04	0	5.22	12.64	21.69	4.85	2.78	3
UCM	6.68	53.8	5.22	0	14.35	21.42	5.98	4.54	4.41
USTHB	13.74	53.32	12.64	14.35	0	25.82	13.12	12.64	12.89
WHU	22.36	58.16	21.69	21.42	25.82	0	20.35	21.26	20.68
Avg Diff	12.48	50.31	11.47	12.02	17.50	23.44	11.70	11.12	11.02

As all the models have an RMS difference greater than this value, the various data selection and field modelling approaches explain the majority differences between the candidate models.

From Table 2, we can observe there are two sets. The first set contains models that are within 7 nT of each other. Candidates BGS, DTU, GFZ, IPGP, MISTA, NOAA, TU Berlin and UCM are in closer agreement with each other and the arithmetic Mean, Median and Huber models. The candidates from CSES, GCRAS, ISTerre, Strasbourg, USTHB and WHU are more scattered with mean differences above 8 nT.

The RMS difference between each model of this first group and the Mean and Median models is below 5 nT. The bottom row of Table 2 gives the arithmetic means of the RMS differences of ${}_{i,j}R$ of model i from the other models j. Again, candidates from the BGS, DTU, GFZ, IPGP, MISTA, NOAA, TU Berlin and UCM teams have small mean differences. Model WHU has the largest mean RMS difference to all models of 14.47 nT, while UCM has the lowest at 5.22 nT. The Median and Huber models in Table 2 have the smallest overall difference between candidates (5.16 and 5.14 nT). As this difference is so small, the Median model, which is straightforward

Table 4 Root-mean-square vector field differences ${}_{ij}R(r)$ at reference radius $r = a$ in units of nT/yr between the various SV-2025–2030 candidate models and between the candidate models and the Mean, Median and Huber SV-2025–2030 models (final three columns). The Avg Diff row is the simple arithmetic means ${}_{i}R$ of the ${}_{ij}R$, where this includes all candidate models

${}_{ij}R$/nT/yr	BGS	CSES	DTU	Edinburgh	GFZ	IPGP	ISTerre	Japan	Leeds	MISTA	NASA
BGS	0	7.73	7.60	22.27	26.68	10.09	7.28	10.92	53.71	7.54	12.77
CSES	7.73	0	2.93	25.48	24.79	9.76	5.12	7.45	55.18	2.84	10.91
DTU	7.6	2.93	0	25.63	24.73	8.79	5.39	6.89	54.73	1.54	11.27
Edinburgh	22.27	25.48	25.63	0	33.3	27.57	24.00	27.88	60.23	25.66	26.58
GFZ	26.68	24.79	24.73	33.3	0	27.41	22.81	25.55	54.48	24.85	25.76
IPGP	10.09	9.76	8.79	27.57	27.41	0	9.76	9.1	54.78	8.38	14.13
ISTerre	7.28	5.12	5.39	24.00	22.81	9.76	0	9.64	54.47	5.20	9.82
Japan	10.92	7.45	6.89	27.88	25.55	9.10	9.64	0	54.86	7.06	13.54
Leeds	53.71	55.18	54.73	60.23	54.48	54.78	54.47	54.86	0	54.91	59.81
MISTA	7.54	2.84	1.54	25.66	24.85	8.38	5.2	7.06	54.91	0	11.34
NASA	12.77	10.91	11.27	26.58	25.76	14.13	9.82	13.54	59.81	11.34	0
NOAA	5.43	3.99	3.81	23.89	25.69	9.69	5.45	8.34	54.19	3.98	11.36
OPGC/LMV	11.23	7.65	7.42	27.64	24.97	11.49	8.6	9.88	55.35	7.32	12.56
Strasbourg	18.84	17.09	16.76	29.61	31.19	17.69	18.06	17.86	53.32	16.87	21.03
TU Berlin	8.78	4.44	3.90	25.33	22.65	9.63	4.9	6.81	53.82	4.14	10.96
UCM	10.27	5.97	6.12	26.84	23.32	11.63	6.20	9.07	55.94	5.93	11.05
USTHB	8.96	5.73	5.62	25.91	25.03	10.07	7.10	8.69	53.37	5.89	12.41
WHU	12.32	12.16	12.68	25.33	29.81	16.39	13.11	14.20	55.35	12.73	15.86
Avg Diff	13.47	11.62	11.43	26.84	26.28	14.80	12.05	13.76	52.14	11.45	16.18

Table 4 (continued)

	NOAA	OPGC/LMV	Strasbourg	TU Berlin	UCM	USTHB	WHU	Mean	Median	Huber
BGS	5.43	11.23	18.84	8.78	10.27	8.96	12.32	6.94	6.88	6.53
CSES	3.99	7.65	17.09	4.44	5.97	5.73	12.16	5.38	2.73	3.04
DTU	3.81	7.42	16.76	3.90	6.12	5.62	12.68	4.99	2.23	2.66
Edinburgh	23.89	27.64	29.61	25.33	26.84	25.91	25.33	23.74	25.05	24.45
GFZ	25.69	24.97	31.19	22.65	23.32	25.03	29.81	22.72	23.99	23.8
IPGP	9.69	11.49	17.69	9.63	11.63	10.07	16.39	9.46	8.54	8.54
ISTerre	5.45	8.6	18.06	4.90	6.2	7.1	13.11	4.92	4.22	3.79
Japan	8.34	9.88	17.86	6.81	9.07	8.69	14.2	8.17	6.82	6.99
Leeds	54.19	55.35	53.32	53.82	55.94	53.37	55.35	51.16	53.85	53.90
MISTA	3.98	7.32	16.87	4.14	5.93	5.89	12.73	5.14	2.30	2.77
NASA	11.36	12.56	21.03	10.96	11.05	12.41	15.86	11.96	10.79	10.4
NOAA	0	8.47	17.72	5.85	7.56	6.18	11.06	4.95	3.55	3.45
OPGC/LMV	8.47	0	19.03	7.57	8.35	8.88	14.49	8.49	7.27	7.43
Strasbourg	17.72	19.03	0	16.9	18.89	16.34	21.23	15.95	16.58	16.47
TU Berlin	5.85	7.57	16.90	0	5.33	6.63	13.51	4.31	3.13	3.13
UCM	7.56	8.35	18.89	5.33	0	8.07	14.69	7.51	5.74	5.83
USTHB	6.18	8.88	16.34	6.63	8.07	0	13.74	5.91	5.02	5.37
WHU	11.06	14.49	21.23	13.51	14.69	13.74	0	12.28	12.31	12.06
Avg Diff	11.81	13.94	20.47	11.73	13.07	12.70	17.15	11.89	11.17	11.15

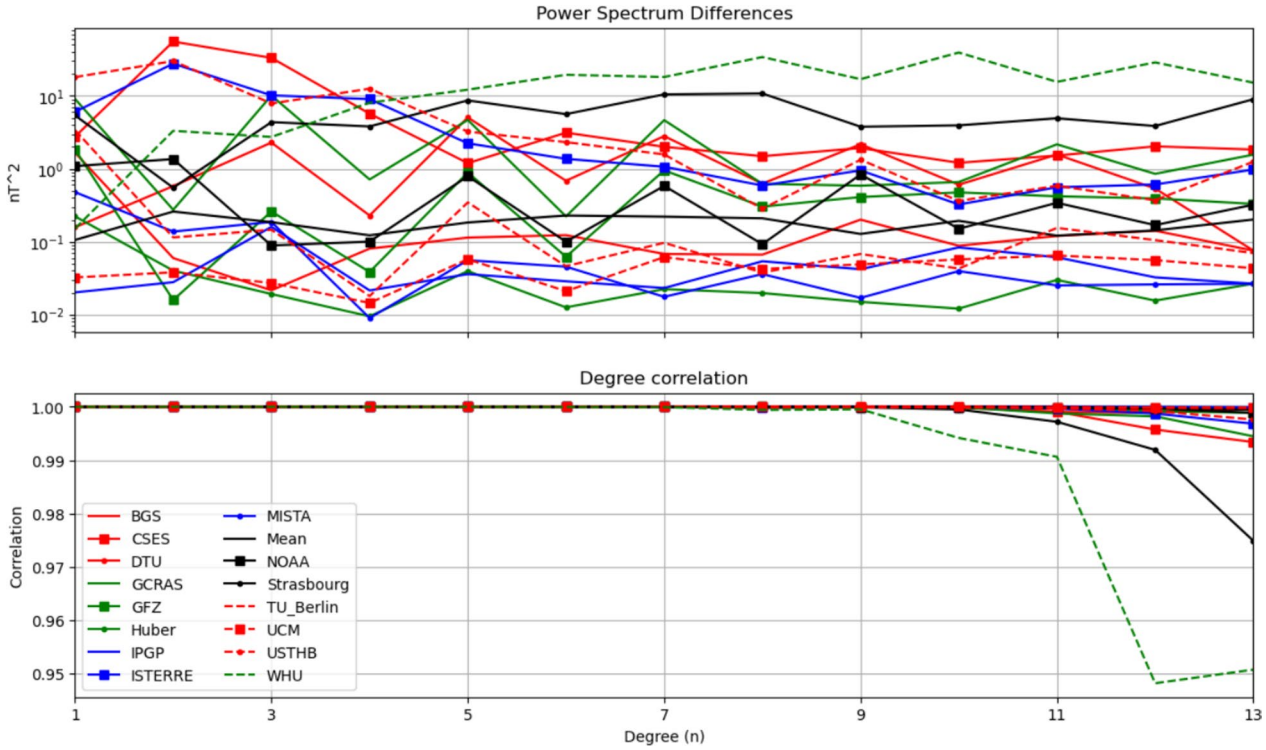

Fig. 1 Power spectrum differences ${}_iR_n(r)$ at reference radius $r = a$ (upper) and degree correlation ${}_{i,j}\rho_n$ (lower) between the DGRF-2020 candidate models and the Median DGRF-2020 model

to compute, is used as the reference in the following comparisons.

Figure 1 (upper) shows the spectral difference per degree (${}_{i,j}R_n$) between the candidate models and the Median model at the reference radius $r = a$. The absolute differences between the candidates and the Median model coefficients are small, with the majority below 0.5 nT. The lower panel shows the correlation per degree. This correlation remains above 0.99 for all candidates until degree 11. Four of the candidate models have slightly reduced correlation at degrees 11 to 13, including the CSES, WHU and Strasbourg models.

Figure 2 illustrates the differences between each candidate model and the Median model for each coefficient plotted as a triangle with degrees in the rows and the $-m$,0,$+m$ in the columns. The difference between most candidate models and the Median model for the zonal coefficients illustrates a problem with the use of satellite measurements related to external fields in the auroral regions. Some teams have accounted for ionospheric currents (e.g. DTU), while others have not, leading to zonal variations, visible along the m=-1,0,1 columns.

Figure 3 shows the differences between the candidate models and the Median model for the vertical (B_Z) component at reference radius $r = a$. The differences are generally small, typically below 5 nT. Some candidates show zonal structure (CSES, WHU) or sectorial differences (ISTerre, USTHB). This figure also shows that the differences between the Mean, Huber and Median models are very small, as could be deduced from Table 2.

For the DGRF model candidates, it is possible to compare their magnetic field predictions directly to Swarm satellite data around 2020.0. We compared each candidate to 1 month of vector data from Swarm A and Swarm B. Using the *viresclient* software tool (Smith et al. 2022), Swarm data were sub-sampled to a rate of 1 sample every 15 s at local times between 00:00 and 05:00. We selected geomagnetically quiet data with Kp < 2 and $|dRC/dt| \leq 4$ nT/h and with QD-latitude below |55°|. Finally, we removed the CHAOS-7 crustal and external field models (Finlay et al. 2020) from the Swarm data. A total of 75,500 measurements were available for the comparison. These core-only vector residuals for the Swarm measurements were compared to each DGRF-2020 candidate model.

Figure 4 shows the B_z residuals of the Swarm data with respect to the DGRF-2020 candidate models as well as with respect to the Mean and Median models. It shows that the Mean and Median models explain the Swarm measurements as well as or better than many of the individual candidates. As a month of data has been used—where the model candidates are a snapshot for the central timepoint—the pattern of the residuals is similar to the

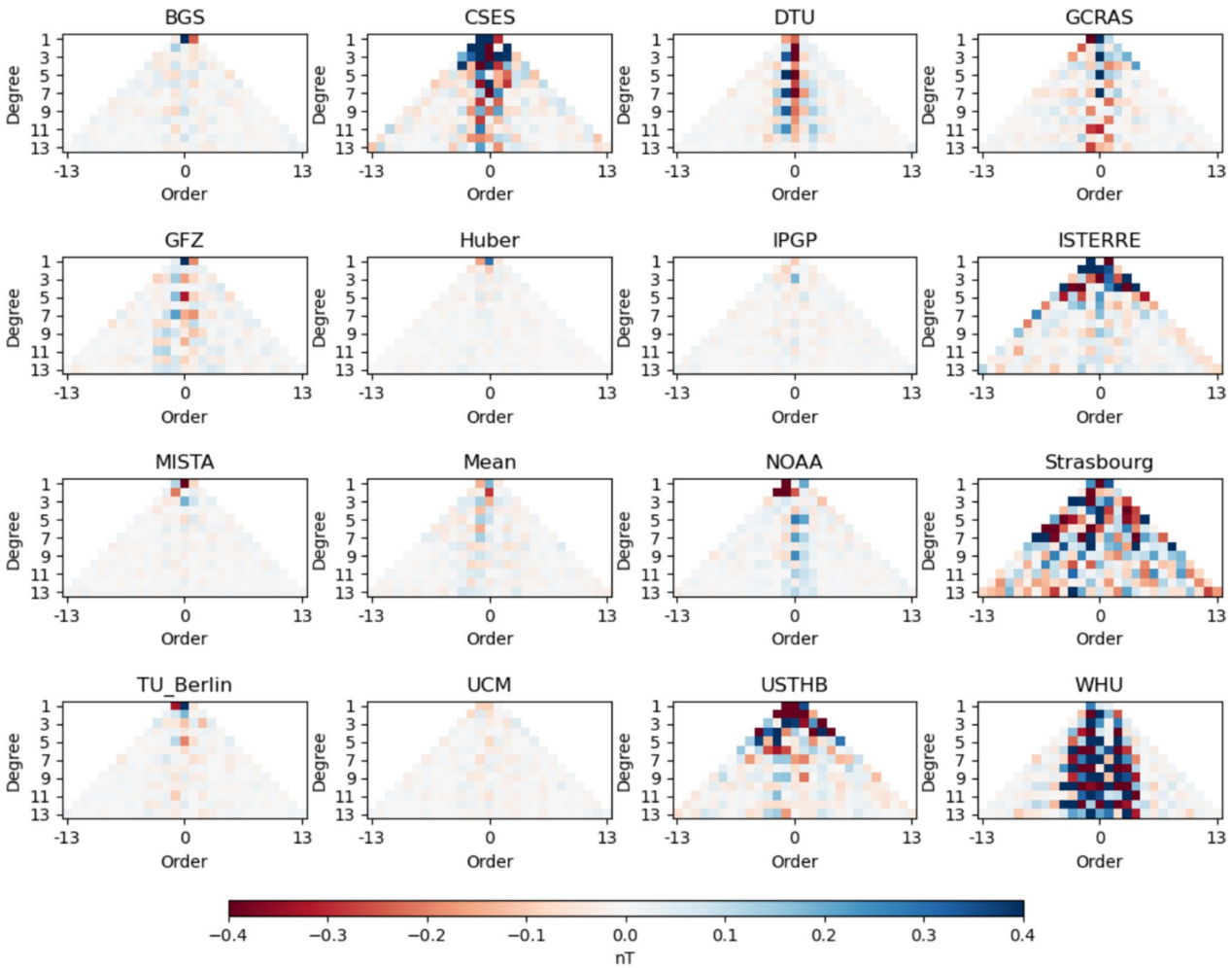

Fig. 2 Gauss coefficient differences as a triangle plot between the DGRF-2020 candidate models and the Median DGRF-2020 model

large scale secular variation of the field. There are also consistent smaller scale features visible (e.g., over Asia) which are likely to be features of the field not captured by models.

Overall, the majority of candidates are very close to each other, though the CSES, ISTerre, Strasbourg and USTHB models stand out as being relative outliers from the others. This can be attributed to the manner in which they were constructed using different techniques or data sets compared to the first cluster. Using the Median (or Huber) method to combine the candidates ensures the (relative) outlier Gauss coefficients are not included directly.

3.2 Analysis of IGRF-2025 candidate models

We performed a similar analysis for the fifteen candidate models submitted to IGRF for epoch 2025.0. Many teams utilized satellite and ground data up to mid to late 2024 for their model calculations. The satellite data sets available were from the ESA Swarm, CSES and the MSS-1 missions, along with quasi-definitive ground observatory vector and scalar data. As magnetic measurements were not available close enough to the desired epoch of 2025.0, the derivation of the main magnetic field candidates for the IGRF model requires a short extrapolation of 3–4 months forward in time.

Most candidates use relatively simple forms of extrapolation (linear SV) from the end-point of their model in late 2024 to extend their main field to 2025.0. This results in a somewhat wider variation of the RMS differences between the Gauss coefficients of the IGRF-2025 candidates compared to the DGRF-2020 candidates (Table 3 to be compared to Table 2). The RMS differences vary between 5 and 15 nT for most models. However, it is the Strasbourg and WHU candidate models that stand out as outliers compared to the others. The Strasbourg model

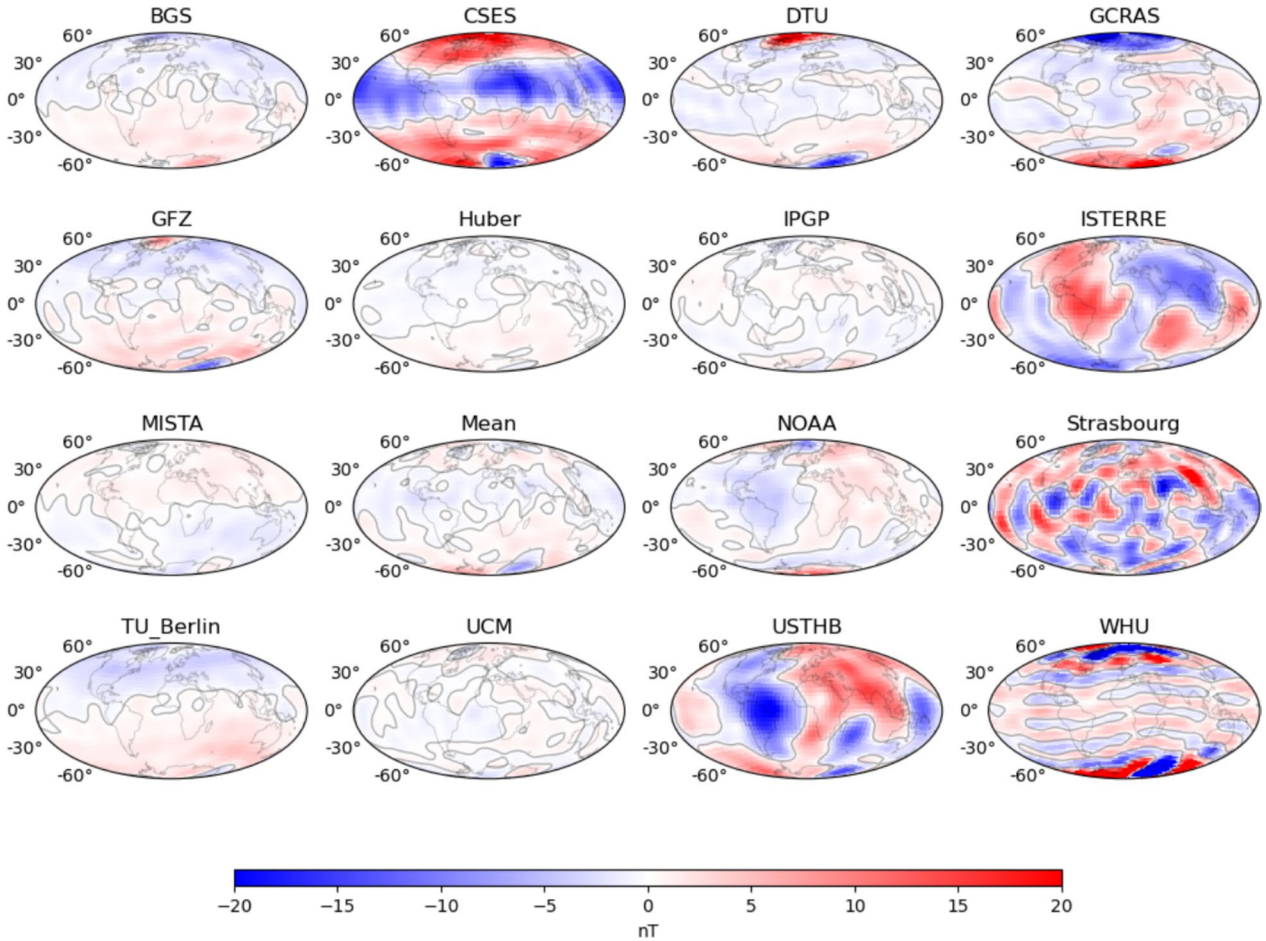

Fig. 3 B_z differences (in nT) between the DGRF-2020 candidate models and the Median DGRF-2020 model at reference radius $r = a$, as well as between the Huber and Mean DGRF-2020 models with respect to the Median DGRF-2020 model. Contour line marks zero value

is substantially different from all others with 53 nT or greater RMS difference. The WHU candidate is closer to the main cluster, though with an RMS difference of more than 20 nT with respect to the other candidates. The difference for the Strasbourg model can be explained by the team's extensive use of ground observatory data in their modelling approach (Wardinski et al. 2026).

The Median and Huber models have lower mean differences compared to the other models, with the Median and Huber models leading to very close values (11.12 nT and 11.02 nT, respectively). The Mean model is slightly further away (11.70 nT) because of the influence of the outlier candidates. We show the Huber model as the reference for comparison in the following figures. Figure 5 (upper) shows the power spectral difference per degree at reference radius $r = a$ between the candidate models and the Huber model (note the logarithmic scale of the y-axis). There is a wider variation in the mean square differences per degree for the IGRF-2025 candidate models than for the DGRF-2020 candidate models (over 300 nT^2 compared to 17 nT^2). The Strasbourg candidate differs across all degrees. The lower panel illustrates the degree correlation which lies above 0.99 until degree 12 for most candidates. The Strasbourg candidate has lower correlation above degree 7, though still remains well-correlated at above 0.92 to degree 13.

Figure 6, analogously to Fig. 2, plots the differences between the candidate Gauss coefficients and the Huber model as a triangle plot. Differences in the individual coefficients have larger values in general compared to what was found in Fig. 2 for the DGRF-2020 candidate models. Most models have an increase in the spectral difference for the zonal $m = 0$ terms. This most likely arises from the treatment of the auroral currents in each model. The WHU candidate has relatively large differences for absolute order up to $m = 5$, but not as large for higher absolute orders.

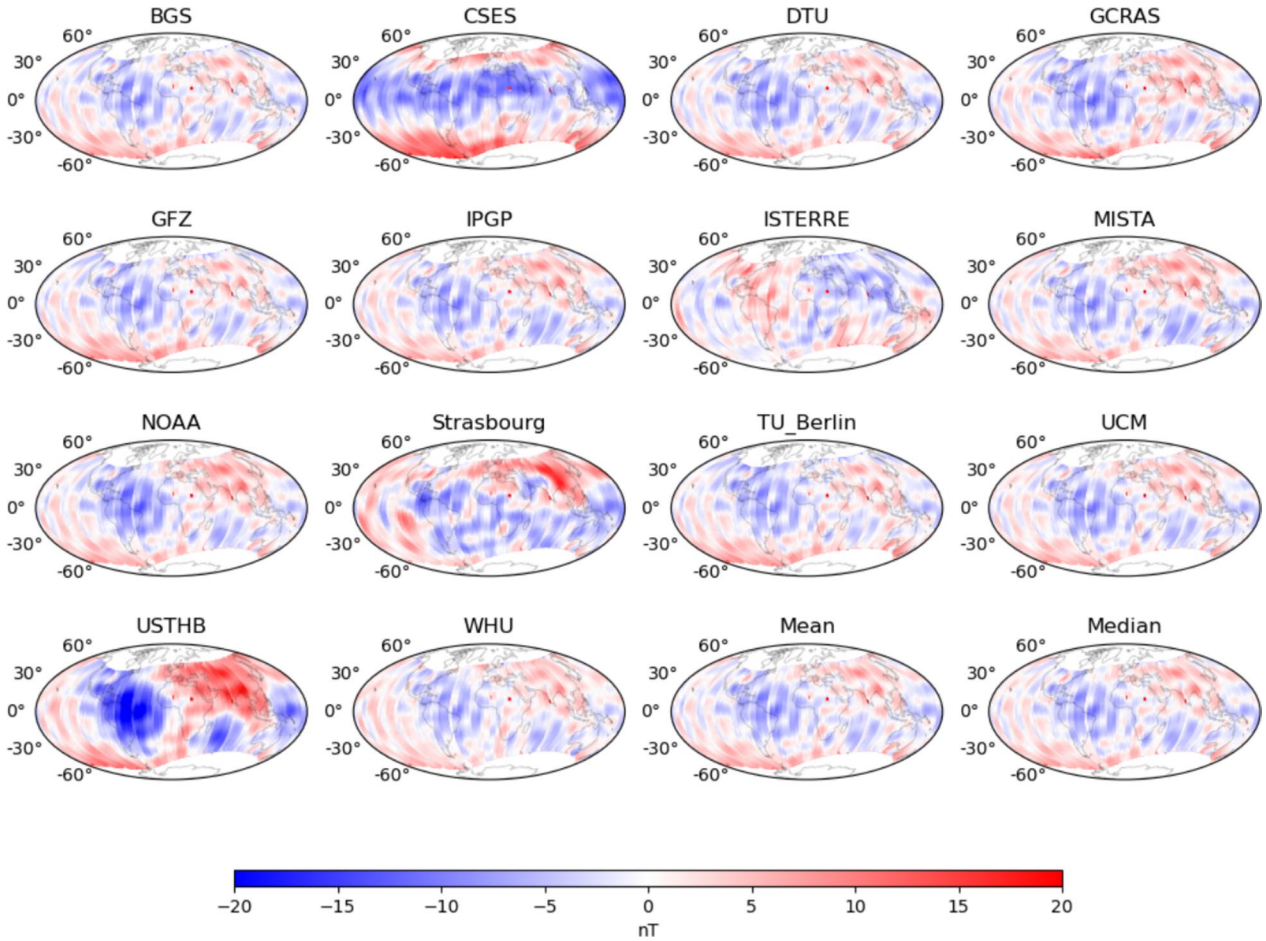

Fig. 4 B_z residuals between a combined Swarm A and B data set and predictions by the DGRF-2020 candidate models and by the Mean and Median DGRF-2020 models. The Swarm data set spans 15 December 2019 to 15 January 2020

Figure 7 shows the differences in the vertical component between the IGRF-2025 candidate models and the Huber 2025.0 model at reference radius, $r = a$. The geographical differences in the north–south hemispherical variations of some candidates arise from the g_1^0 coefficient. The maps also show the effects of the extrapolation to 2025.0 as the scale bar is now ±50 nT (cf. ±20 nT for Fig. 3). Some models have an obvious sectorial or hemispherical difference, such as BGS, GFZ, MISTA, OPGC and UCM, while the GCRAS and WHU candidates show large differences at the polar and auroral zones. The Strasbourg candidate again has the largest differences globally compared to the Huber model.

After the release of the IGRF-14 in November 2024, it was possible to collect measured data to compare against the candidate models. Figure 8 shows maps of residuals between the candidates and Swarm data. These were constructed using 1 month of measurements centered on 01-Jan-2025 from Swarm Alpha and Bravo. The data were corrected from the high spherical harmonics degree core field (from degree 14 to 20), the lithospheric field, and the magnetospheric field using the CHAOS-8.3 geomagnetic model. To minimize the effect of ionospheric fields, we also corrected the data from E-region ionospheric fields using the extended DIFI model (Chulliat et al. 2016). Note, this differs from the pre-processing in Fig. 4, in which data were selected for quiet night-time only.

We next removed outliers using a generalized extreme Studentized deviate test for outliers with an upper bound of 10% of the number of data in the data set. This was done separately for high-latitude data (quasi-dipole latitude above 55° in the two hemispheres) and mid- and low-latitude data (quasi-dipole latitude between |55°|). Finally, the data were selected for geomagnetic quiet times using Hp30<2. The comparisons show small differences for most candidates. The residuals may relate mainly to unmodelled ionospheric effects. The Huber model matches most closely to the Swarm data, better than any individual candidates, which implies (post-hoc)

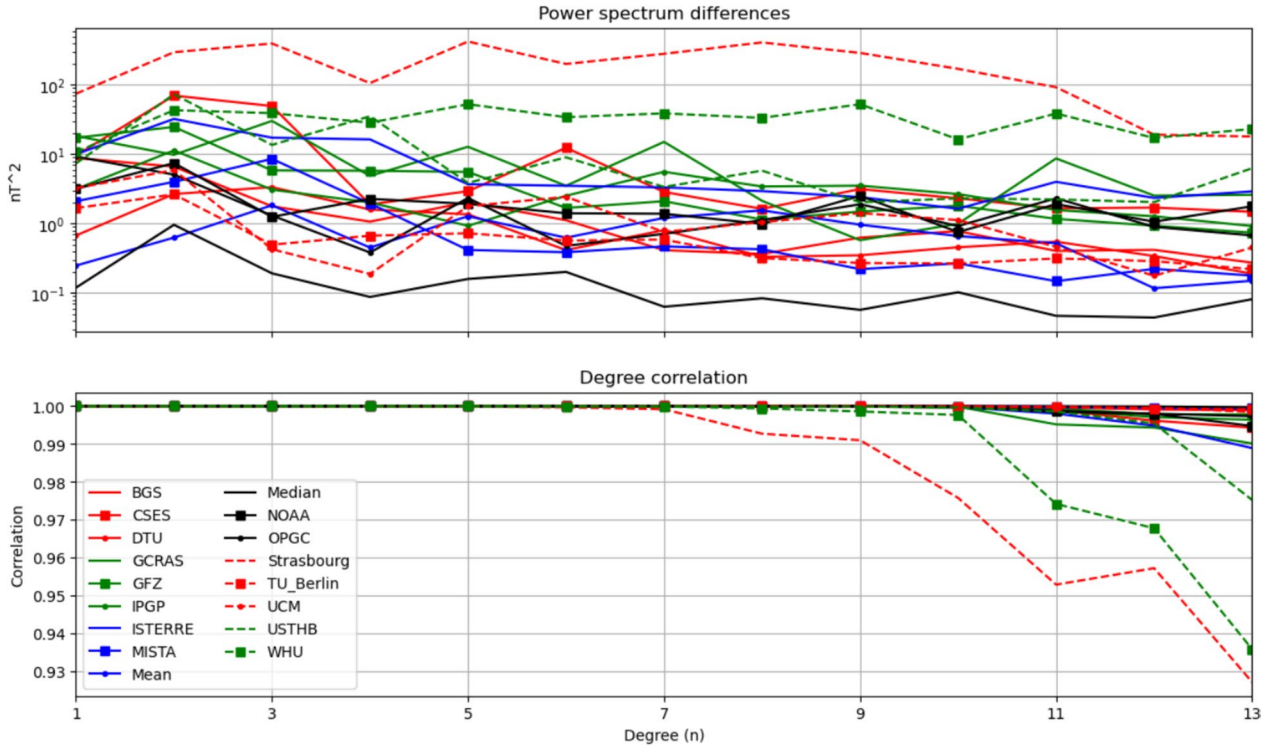

Fig. 5 Power spectrum differences ${}_iR_n(r)$ at reference radius $r = a$ (upper) and degree correlation ${}_{i,j}\rho_n$ (lower) between the IGRF-2025 candidate models and the Huber IGRF-2025 model

the final IGRF-2025 model is an excellent description of the field at 2025.0.

3.3 Analysis of IGRF-14 SV-2025–2030 candidate models

Eighteen teams submitted candidate models for the predicted rate of change in the 2025–2030 time period. For these models, teams submitted coefficients $\dot{g}_n^m, \dot{h}_n^m$ to spherical harmonic degree and order 8, to represent the average change in the Gauss coefficients between 2025 and 2030 in units of nT/year. The institutes which led the different SV candidate models are also noted in Table 1.

There are a variety of approaches for forecasting secular variation. The BGS candidate uses core flow modelling with steady flow and acceleration, while the CSES, DTU, GCRAS and UCM used extrapolation of measured secular variation from the previous year or longer. Three teams (GFZ, Japan and Leeds) adopted machine learning approaches to forecasting secular variation. Rother et al. (2026) used machine learning on the Gauss coefficients directly to determine patterns of variation over time. Sato et al. (2026) used machine learning on the flow acceleration to deduce the underlying temporal pattern of change in spherical harmonic coefficients. Shakespeare-Rees et al. (2026) used a Physics-Informed Neural Network (PINN) to determine local core flow and then to compute the global secular variation from the advected flow.

Madsen et al. (2026) performed a similar type of analysis to Sato et al. (2026), though they determined the flow acceleration coefficients to be controlled by sinusoidal variation on different time periods rather than search for a more complex pattern using machine learning. Other teams, such as the NASA (Gwirtz et al. 2025), ISTerre (Claveau et al. 2025) and IPGP candidates, adopted data assimilation in combination with geodynamo models to infuse measurements into sophisticated models of the core behavior to create a physics-based forecast.

The SV candidate models offer a diverse set of approaches to compute field change over the period 2025.0 to 2030.0 which produces a wide variation between the candidates, as shown in Table 4. The candidate differences fall into three clusters: (i) those that match each other to within 12 nT/yr, (ii) those whose differences are greater than 20 nT/yr and (iii) one that exceeds 50 nT/yr. The candidates most different from the rest of the population are the Leeds, Edinburgh and GFZ models. Shakespeare-Rees et al. (2026) later identified a transcription error in the submitted Leeds candidate of September 2024 which is the reason for the large differences. Their paper describes the corrected version of the SV candidate; however, this analysis uses the original submission.

The RMS values of the Mean, Median and Huber models computed from the candidates have an average

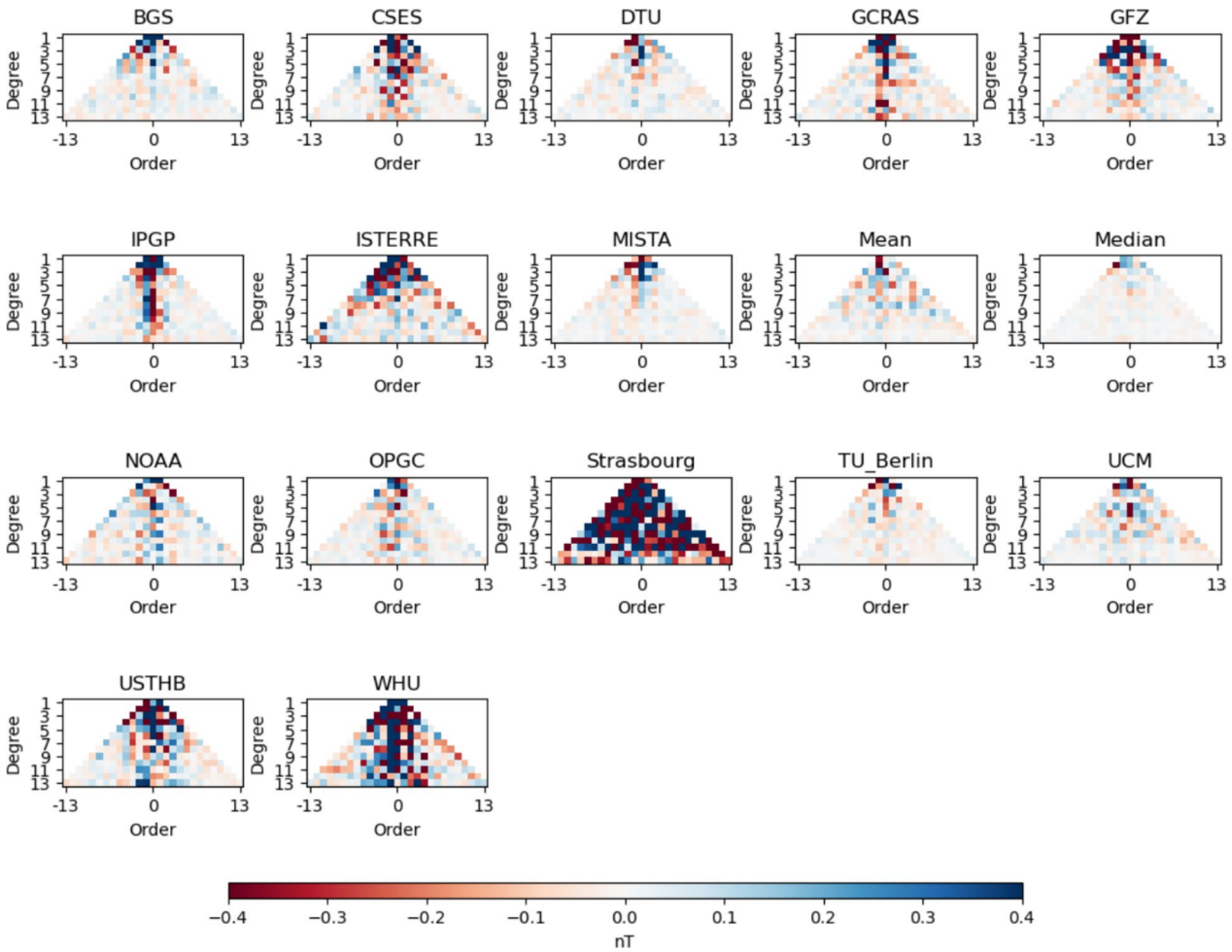

Fig. 6 Gauss coefficient differences as a triangle plot between the IGRF-2025 candidate models and the Huber IGRF-2025 model

difference of around 11 nT/yr (last three columns of Table 4). By computing the Huber model, candidates that show large-scale differences are down-weighted. The maps of the weights are complex, as different candidates are higher in some regions of the globe than others. In the final Huber-weighted model the contribution of any particular candidate is mixed across Gauss coefficients.

We show maps of the differences in the vertical component of the candidates to the Huber model in Fig. 9. The Edinburgh, GFZ and Leeds models are the most different from the other forecasts with large hemispherical difference in the Leeds model which can be traced to the negative sign of the g_1^0 compared to the other candidates. The Strasbourg model has higher degree and order differences, while the WHU model shows largest variations in the polar regions. The IPGP, ISTerre, NASA and Japan candidates are close to the consensus model, showing the data assimilation and machine learning methods can produce similar looking model outputs.

4 Taskforce decision on IGRF-14 candidate combination

The analysis of the submitted candidates shows that most were very similar to each other and within the expected variation from data selection, processing and modelling methodologies based on experience of previous IGRF generations. For each final model, the Taskforce suggested and then voted on up to three methods for combining the candidates. For the DGRF, IGRF and SV models, members of the Taskforce voted on their preferred method of combination and the majority vote was chosen in all cases.

For the DGRF-2020 the Gauss coefficients of Mean, Median and Huber models are extremely close to each other at just over 5 nT RMS difference on average with the other candidates. Despite the Huber model having a very slightly lower mean difference to the candidates, the Median model was voted by the Taskforce as their preferred method, as it is the most straightforward to compute.

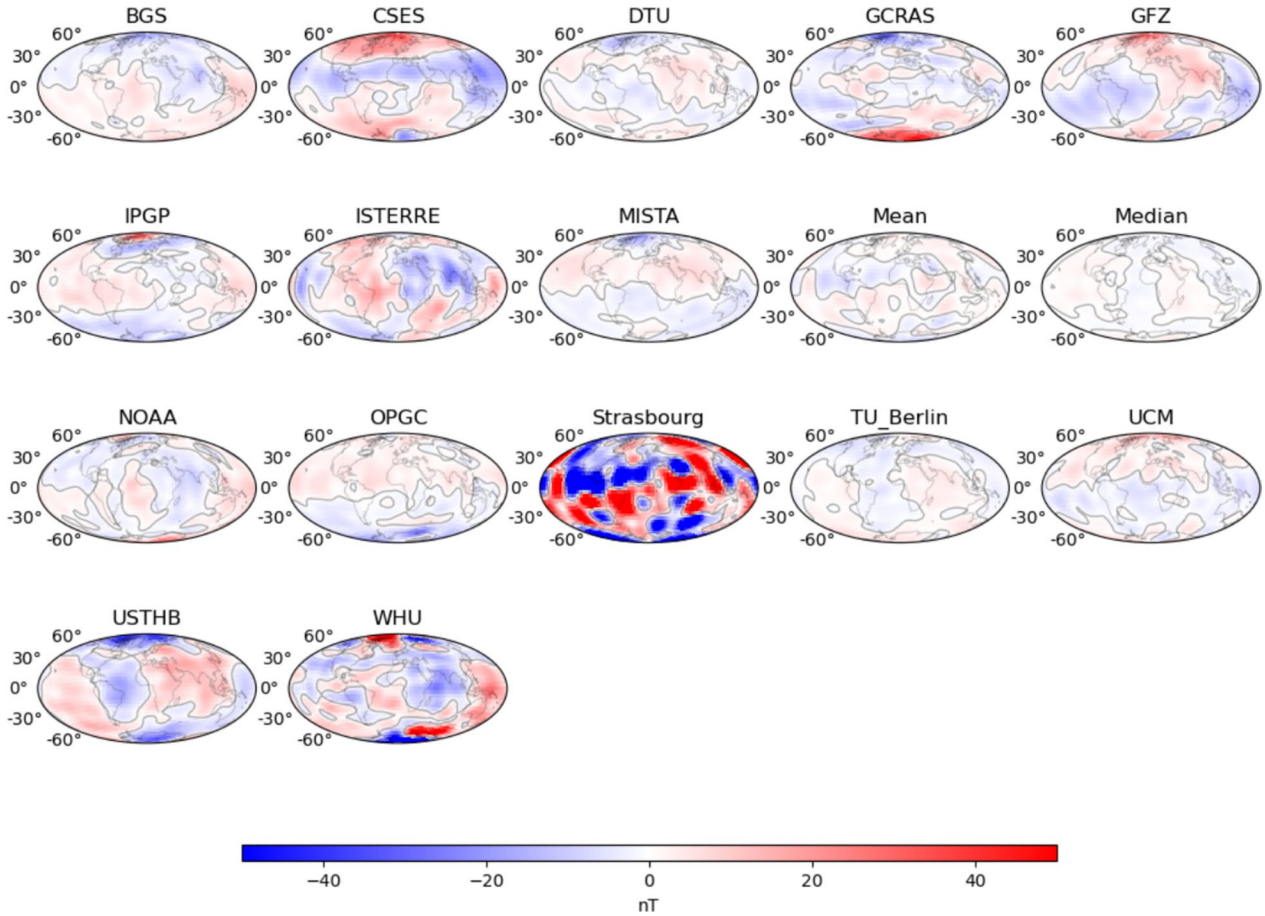

Fig. 7 B_z differences (in nT) between the IGRF-2025 candidate models and the Huber IGRF-2025 model at reference radius $r = a$, as well as between the Mean and Median IGRF-2025 models with respect to the Huber IGRF-2025 model. Contour line marks zero value

For the IGRF-2025 and the SV-2025–2030 candidates there was a wider divergence in the candidates with larger differences between the more extreme ranges of the forecasts. The Taskforce analysis suggested that the Huber-weighted model produced a better representation of the variation without biasing the model toward the most different candidates. The majority vote selected the Huber-weighted model for the IGRF-2025 and SV-2025–2030 models as a fair representation of the variation and allows all candidates to contribute to the final Gauss coefficients.

4.1 Alternative analyses of IGRF-14 candidates

Along with the standard and well-established methods of comparison for candidates, we briefly show three other types of analysis. Clustering of coefficients can be determined by examining the candidate Gauss coefficients and determining the principal components of the scatter between models (Ramsay and Silverman 2005; Bishop and Nasrabadi 2006). This reveals candidates which are close together, for example. In Fig. 10, we show the scatter between the 1st and 2nd components of the DGRF, IGRF and SV candidate models.

The DGRF candidates (upper panel) are very close with a small level of scatter except for the four outliers noted above lying further away. The IGRF candidates (central panel) show a central cluster with a wider scatter along the PCA2 component. Two models (Strasbourg and WHU) fall well outside the main set of candidates in orthogonal directions. The analysis of the SV candidates (lower panel) shows a cluster away from the mean with three models (Leeds, Edinburgh and GFZ) being separate from the others. Two of these are the machine-learning-based methods and the Edinburgh candidate which uses fitting of sinusoidal functions to past acceleration of the core flow to predict future SV.

The IGRF models are often used in studies of the field at the core–mantle boundary (CMB). Figure 11 illustrates

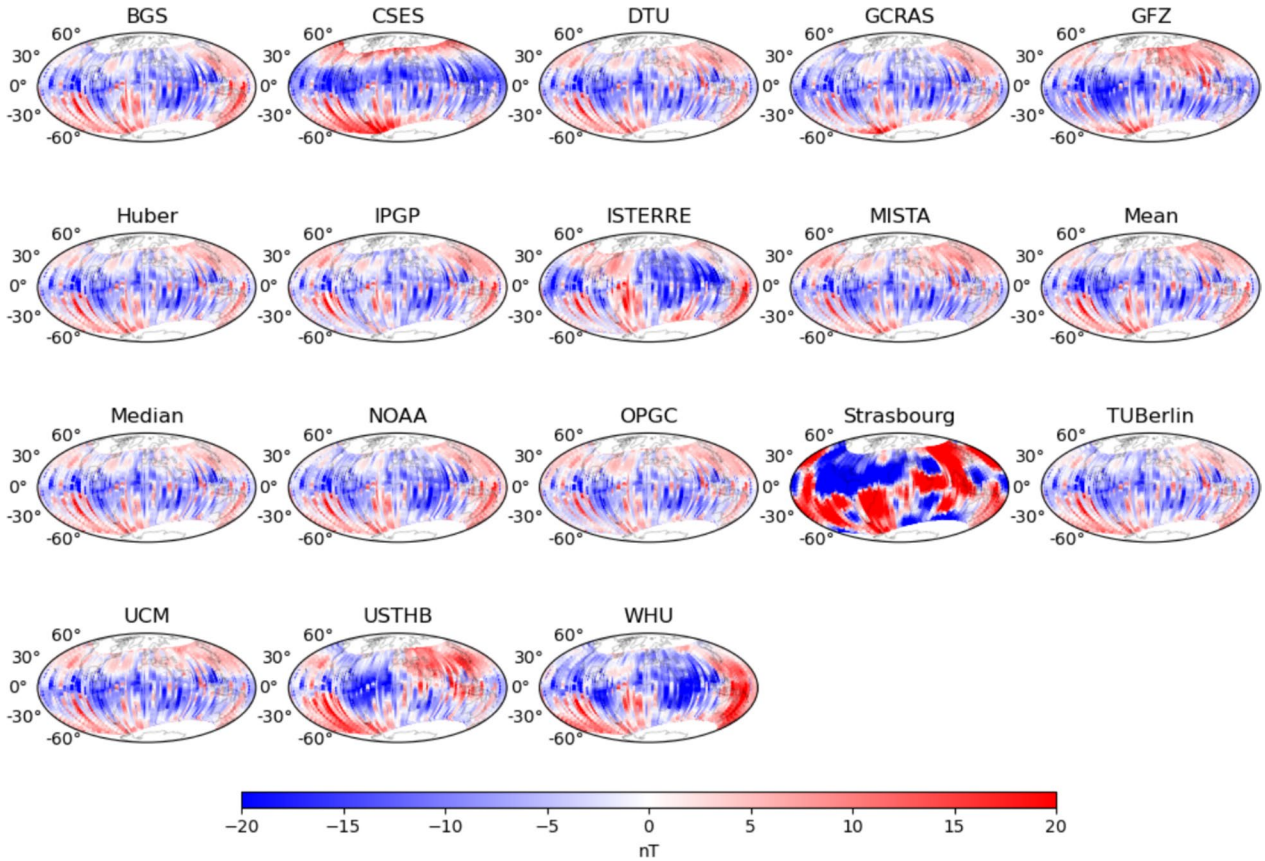

Fig. 8 B_Z residuals between a combined Swarm A and B data set and predictions by the IGRF-2025 candidate models and by the Huber, Mean and Median IGRF-2025 models. The Swarm data set spans 15 December 2024 to 15 January 2025

the variability of the candidates by plotting the null flux curve, where B_r=0 on the CMB. The upper panel shows the DGRF for 2020.0 which shows very consistent contours between the models, including the reversed patch associated with the South Atlantic Anomaly. The only obvious difference is in the central Atlantic patch, east of the Caribbean, where some models have a larger extent than others. The lower panel shows the IGRF candidates at 2025.0 which display a greater variation in contour locations. In particular, the reversed patches south of the African continent have merged in the majority of models but not all. The central Atlantic patch has merged in one model (WHU), though it is still separated in the remainder.

Finally, we look at the predictions of the SV for one location close to the South Atlantic Anomaly at the Vassouras observatory (Brazil). Figure 12 shows the annual differences of the monthly means derived from the observatory data in the magnetic X (North), Y (East) and Z (Down) components from 2010 to 2024.25. The SV predictions from past candidates for IGRF-13 and this generation are shown. Most candidates cluster around similar SV in dY/dt but there is a wider set of estimates in dX/dt and dZ/dt. In particular, the GFZ model is quite separate, predicting -70 nT/yr compared to -110 nT/yr for many of the other candidates. The 15th generation revision (in 2030) should allow the discrimination of the best candidate or modelling approach.

5 Discussion

We point out some issues we found with the process for computing the final coefficient values. For the DGRF-2020 and IGRF-2025 coefficients, all candidate models were rounded to two decimal places, which was the format requested for submission to the GitHub repository. For DGRF-2020, the Median model was computed and output to two decimal places. However, as there are an even number of models, the median is the average of the two central coefficient values when sorted, which occasionally produces a result with three decimal places. The coefficients with three decimal places of resolution were subsequently rounded to two decimal places before being

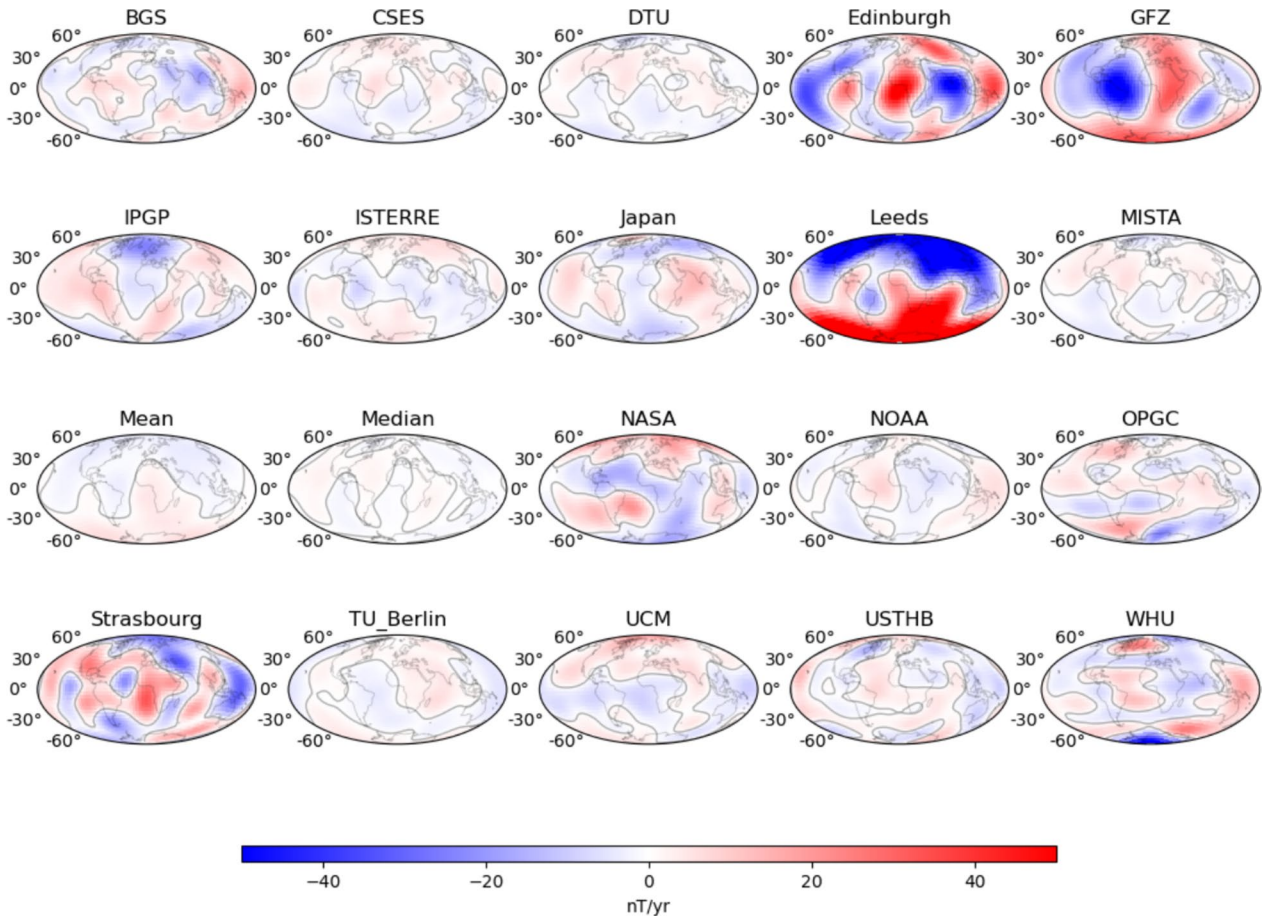

Fig. 9 dB_z/dt differences (in nT/yr) between the SV-2025–2030 candidate models and the Huber SV-2025–2030 model at reference radius $r = a$. Also shown are the differences between the Mean and Median SV-2025–2030 models with respect to the Huber SV-2025–2030 model. Contour line marks zero value

output. The IGRF-2025 and SV-2025–2030 Huber models were computed and then rounded to one decimal place.

5.1 Rounding behavior

During the process we detected a discrepancy between Python-created coefficient files and those made by Matlab and the conventional Fortran code which has underpinned much of the IGRF modelling since the 1980s. The issue relates to the manner in which different code packages round from two to one decimal place for the IGRF and SV coefficients.

Traditionally, geophysicists tend to use 'round away from zero'. When '5' is the last significant digit with two decimal places, for example, −2.65 becomes −2.7. However, the Python3 *numpy* package instead rounds to the nearest even decimal digit (also called 'banker's rounding'). In this scenario, −2.65 rounds to −2.6 but −2.75 rounds to −2.8. The advantage of banker's rounding (for accountancy) is that there is no net increase in the total value of the sum of the rounded numbers, which makes sense for financial transactions. The rounding difference between Python and Fortran affected nine coefficients in total in the IGRF and SV coefficients. To resolve the behavior, a Python function was created to force 'round away from zero' to remain consistent with previous generations and the coefficient files were checked to ensure they were correct. These unexpected issues demonstrate the value of cross-checking outputs to ensure consistency in different implementations and computer languages.

5.2 Future improvements

With the expected continuation of high-quality satellite missions providing data coverage that already allow IGRF and DGRF models to be built up to spherical harmonic degree and order N=13, the question arises whether the predictive secular variation model also provided with each new IGRF release could also be provided to the same degree and order N in the future. Most of the

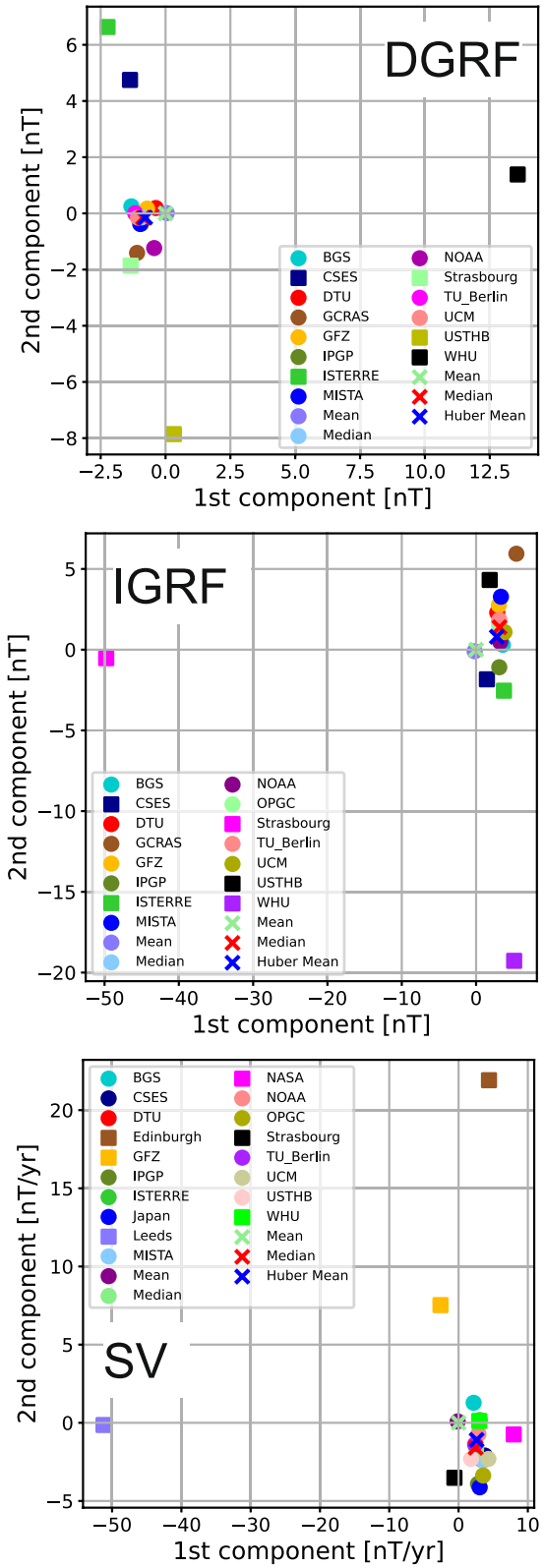

Fig. 10 Scatter of PCA1 versus PCA2 for the DGRF, IGRF and SV candidates. See text for details

IGRF-14 SV candidate models analysed were already extracted from the same time-varying parent models used to produce DGRF-2020 and IGRF-2025 candidate models up to N=13, and all could have technically been provided up to that order and degree.

This is a path that has already been followed by the analogous World Magnetic Model (WMM) developed for operational purposes and with more specific requirements than IGRF (Chulliat et al. 2025). WMM provides a field model at epoch 2025.0 and a predictive secular variation, both to degree N=12. More generally, the benefit of having a higher spatial resolution description of the SV is also well-known for core dynamics investigation, especially when it comes to recover core surface flows (Hulot et al. 1992; Eymin and Hulot 2005), as again recently noted by (Rogers and Mandea 2026).

Past discussions within the IAGA Division V-MOD Working Group on the topic focussed on the issues a change in N would introduce were continued satellite observation of the magnetic field from low Earth orbit not maintained. The community would be forced to go back to using data from the sparsely distributed ground observatory network. Presently, the maximum resolution possible from ground-only data is degree and order N=8, which is why IGRF predictive secular variation models are provided to N=8.

Such a concern is now fading with many missions currently in orbit and likely to remain operational for some significant time. Willingness of space agencies to ensure this is, for instance, illustrated by the decision of ESA in November 2025 to extend operation of the Swarm mission at least up to 2029, with the hope that the ESA Swarm Bravo satellite could remain operational far beyond that date. In addition, new missions are already planned or are under active development, such as the ESA Scout NanoMagSat mission to be launched in 2027 (Deconinck et al. 2025). The low cost of this and other new (nano-)satellite missions will encourage maintenance of the long-term observations from space, as supported by IAGA resolution 2025 (1) (see https://iaga-aiga.org/resolutions/res1-25/).

We further note that additional satellite missions can allow a wider variation of different data sources to be used in the creation of new candidates. This will also be useful for evaluation of future IGRF candidate models by comparing them with data that were not used for model construction. This would help provide further information on bias and variance between different missions, separate from the model differences introduced by methodology and data selection.

As the analysis of the IGRF-14 SV-2025–2030 candidate models showed, improvement is also much needed to make such models more accurate even up to the

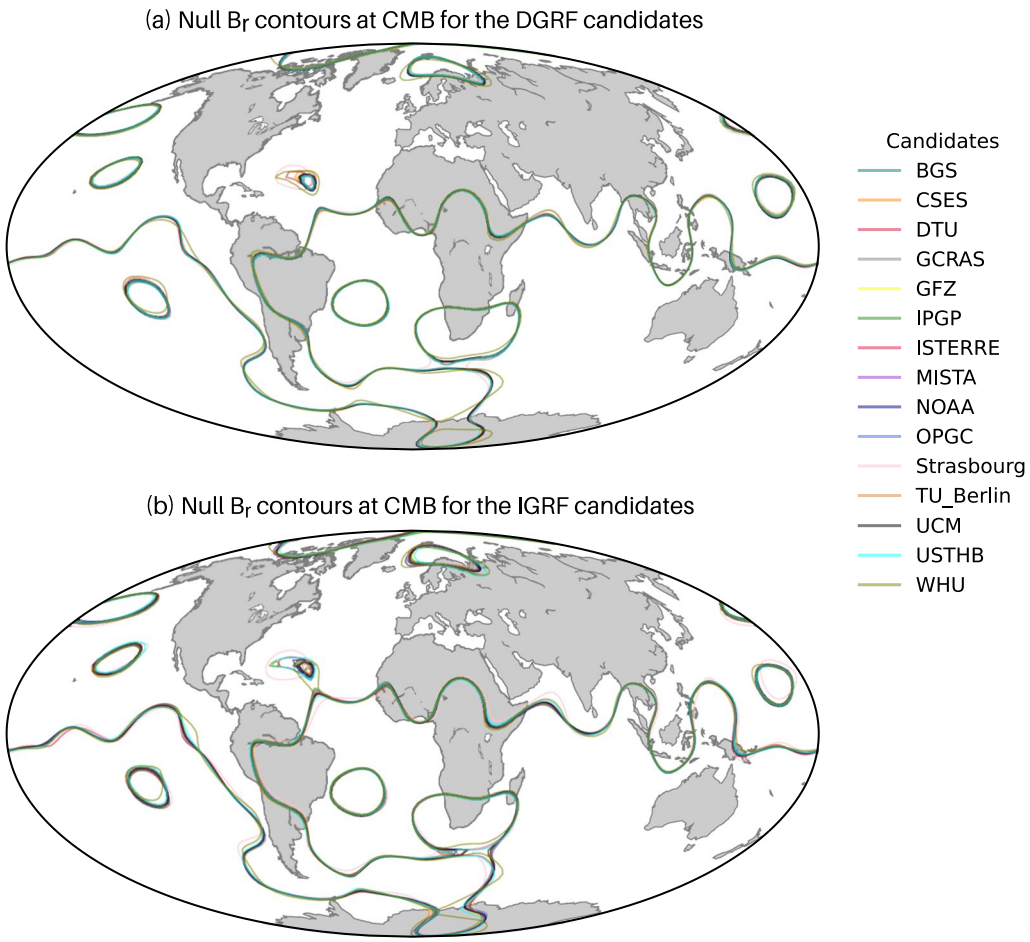

Fig. 11 Comparison of the null flux curves ($B_r = 0$) of the (a) DGRF and (b) IGRF candidates at the core–mantle boundary. Continents for reference only

degree and order N=8 already provided. The issue is not so much with the possibility of building accurate SV models from the data but more with the issue of defining the right strategy to build a predictive model that remains sufficiently accurate over the following 5 years. The intrinsic impossibility of making any detailed prediction of the core magnetic field even on medium term is a well-known limitation (Hulot et al. 2010) but this does not fundamentally affect the feasibility of making better 5 year short-term predictions needed for IGRF purposes.

Unfortunately, no robust strategy has yet been found, as demonstrated by e.g., retrospective performance analysis of past IGRF SV predictive candidate models (Finlay et al. 2010; Alken et al. 2021b) and as pointed out in recent investigations of how a better strategy could be found (Gillet et al. 2024). The key issue to be solved relates to the fact that the secular variation is not stationary and that sudden changes, can occur within a few years, in a presently unpredictable manner. The nature and cause of such sudden changes which often occur in the form of secular acceleration pulses that affect all scales of the secular variation (Chulliat et al. 2010) are just beginning to be understood, thanks to advanced numerical simulations (Aubert and Finlay 2019) and improvements in data quality from Swarm (e.g. Madsen et al. 2025).

Significant efforts are thus still required to find an adequate strategy to correctly predict the average secular variation over 5 years, as needed for IGRF releases. It is our hope that such a strategy may be found for the next IGRF-15 release in 2030 for the benefit of all IGRF users.

6 Conclusions

A total of 19 international teams submitted candidates for consideration for the 14th generation of the International Geomagnetic Reference Field (IGRF-14). The teams submitted fourteen candidate main field models for the definitive (DGRF) epoch 2020.0, fifteen candidate main field models for the IGRF epoch 2025.0, and eighteen secular variation (SV) models for the forecast period

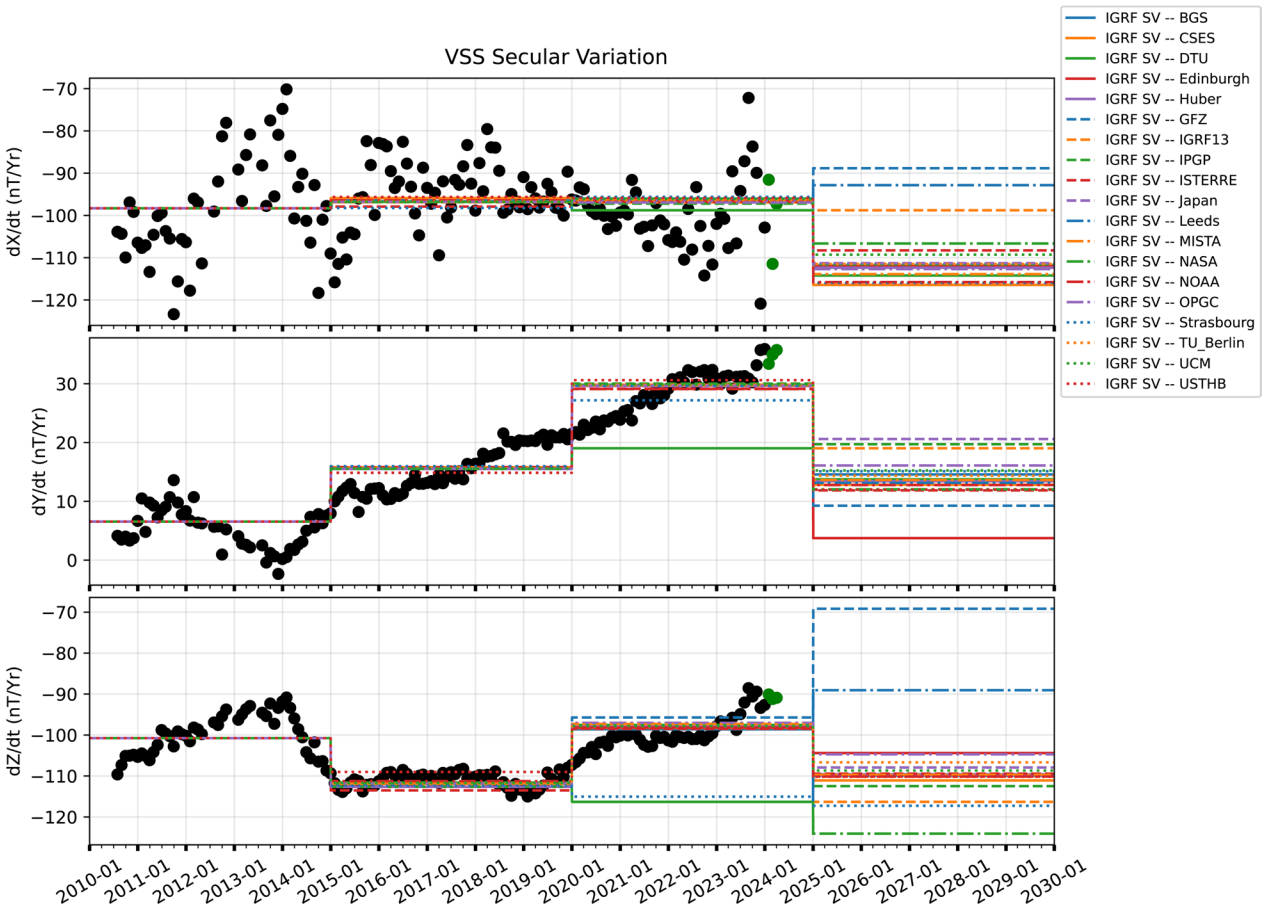

Fig. 12 Secular variation (SV) predicted by candidate models (lines) and estimated from Vassouras (VSS) observatory data (dots). Black dots represent SV values from Swarm AUX_OBS_2 data, while green dots correspond to SV derived directly from VSS data. Candidate models use DGRF, IGRF, and SV model coefficients for 2020, 2025, and 2030, respectively, where available. For candidates without DGRF or IGRF coefficients, IGRF-13 is shown

covering 2025.0 to 2030.0. The 47 submitted candidates were thoroughly analyzed to deduce the best methodology for combining them into a final set of models for release.

A voluntary Taskforce consisting of the authors of this paper carried out their analyses separately, reporting back to the IAGA DIV V-MOD chair and co-chair. The analyses used both spectral and spatial comparisons, and comparisons to independent data sets. Their conclusions were used to guide the votes on the best method for computing the final spherical harmonic coefficients for each product.

The IAGA IGRF Taskforce voted to use the median of the DGRF-2020 candidates as the final model, and a spatial Huber iteratively reweighted scheme of the candidates for the IGRF-2025 model and SV-2020–2025 model. The final model coefficients were released in November 2024 and are freely and publicly available.

Acknowledgements

We acknowledge the indirect contributions from the many scientists, support staff, engineers and observers who support magnetic measurements and research. The European Space Agency (ESA) is gratefully acknowledged for providing access to the Swarm magnetic field data. Macao Foundation (MF) and China National Space Administration (CNSA) are gratefully acknowledged for providing MSS-1 satellite data. The results presented in this paper rely on data collected at magnetic observatories. We thank the national institutes that support them and INTERMAGNET for promoting high standards of magnetic observatory practice (www.intermagnet.org). This paper is published with the permission of the Director of the British Geological Survey (UKRI).

Authors Contributions

CB (BGS) is chair of the IAGA DIV V-MOD (2023–2027) and initiated, coordinated and organised the call and delivery of the 14th generation of the IGRF. CK (DTU) is co-chair (2023–2027). CB and CK co-wrote the manuscript based on the analyses of the contributing co-authors. A. Smith contributed to the creation and maintenance of the GitHub and Zenodo repositories. Figure 9 was generated from data provided by MF (IPGP) and Fig. 10 with code written by SN (ISM, Japan). Figure 11 was generated by FT-N (Nantes) and Fig. 12 by MS (GFZ). All authors contributed detailed technical analyses forming the results presented. All co-authors have contributed, read and approved the manuscript.

Funding
The French contribution to this work was supported by the French Centre National des Etudes Spatiales (CNES) in the framework of the program "Exploitation de la mission satellitaire européenne Swarm".

Data availability
The IGRF-14 candidate models and evaluation code (GitHub repository) are available at: https://github.com/IAGA-VMOD/IGRF14eval and Beggan et al. (2024). The final coefficients of IGRF-14 in ASCII format: https://www.ngdc.noaa.gov/IAGA/vmod/coeffs/igrf14coeffs.txt and the coefficients of IGRF-14 in a Zenodo repository https://zenodo.org/records/14218973 (International Association of Geomagnetism and Aeronomy 2024). ESA Swarm magnetic field data are available at https://swarm-diss.eo.esa.int/. They were accessed using the VirES client Python tool (Smith et al. 2022). Definitive ground-based geomagnetic observatory data are available from INTERMAGNET (https://intermagnet.org) or the World Data Centre for Geomagnetism (https://wdc.bgs.ac.uk). Other satellite data used in the creation of the IGRF candidates models were: Cryosat-2 data are available from https://earth.esa.int/web/guest/swarm/data-access. Swarm ASM-V experimental data are available from https://dataverse.ipgp.fr/dataverse/swarm-data. CHAMP data can be obtained from http://isdc.gfz.de. Ørsted and SAC-C data are available from https://www.space.dtu.dk/english/research/scientific_data_and_models/magnetic-satellites. CSES data are available from http://www.leos.ac.cn. Macau Science Satellite data are available from: https://mss.must.edu.mo/.

Declarations

Competing interest
The authors declare that they have no competing interest.

Author details
[1]British Geological Survey, Lyell Centre, Research Avenue South, Edinburgh EH14 4AP, UK. [2]Division of Geomagnetism and Geospace, DTU Space, Technical University of Denmark, Centrifugevej 356, Kongens Lyngby 2800, Denmark. [3]Institute of Geophysics and Meteorology, University of Cologne, Albertus-Magnus-Platz, Cologne 50923, Germany. [4]Cooperative Institute for Research in Environmental Sciences, University of Colorado Boulder, 325 Broadway, E/NE42, Boulder 80305, CO, USA. [5]NOAA National Centers for Environmental Information, Boulder, CO, USA. [6]Institute for Astronomy, Astrophysics, Space Applications and Remote Sensing, National Observatory of Athens, 15236 Athens, Greece. [7]Université Paris Cité, Institut de physique du globe de Paris, CNRS, 75005 Paris, France. [8]Laboratoire Magmas et Volcans, OPGC, IRD, CNRS, Université Clermont Auvergne, Aubiére, France. [9]GFZ Helmholtz Centre for Geosciences, Telegrafenberg, 14473 Potsdam, Germany. [10]Department of Earth and Space Sciences, Southern University of Science and Technology, 518055 Shenzhen, China. [11]Department of Earth and Planetary Sciences, Institute of Science Tokyo, Tokyo 152-8551, Japan. [12]Department of Earth and Planetary Sciences, Graduate School of Science, Kobe University, Kobe 657-8501, Japan. [13]The Institute of Statistical Mathematics, School of Statistical Thinking, Tokyo 190-8562, Japan. [14]Facultad de Ciencias Físicas, Departamento de Física de la Tierra y Astrofísica, Madrid 28040, Spain. [15]Instituto de Geociencias IGEO, Madrid, Spain. [16]Division of Earth and Planetary Sciences, Graduate School of Science, Kyoto University, Kitashirakawa Oiwake-cho, Sakyo-ku, Kyoto 606-8502, Japan. [17]School of GeoSciences, University of Edinburgh, Edinburgh EH9 3BA, UK. [18]Nantes Université, Univ Angers, Le Mans Université, CNRS, Laboratoire de Planétologie et Géosciences, LPG UMR 6112, Nantes 44000, France. [19]Institut Terre & Environnement de Strasbourg, Ecole et Observatoire des Sciences de La Terre, Université de Strasbourg, CNRS, UMR 7516, Strasbourg, France. [20]School of Electronic Information, Wuhan University, Wuhan, China.

Received: 20 October 2025 Accepted: 27 January 2026
Published online: 29 June 2026

References

Alken P, Thébault E, Beggan CD, Amit H, Aubert J, Baerenzung J, Bondar TN, Brown WJ, Califf S, Chambodut A, Chulliat A, Cox GA, Finlay CC, Fournier A, Gillet N, Grayver A, Hammer MD, Holschneider M, Huder L, Hulot G, Jager T, Kloss C, Korte M, Kuang W, Kuvshinov A, Langlais B, Léger JM, Lesur V, Livermore PW, Lowes FJ, Macmillan S, Magnes W, Mandea M, Marsal S, Matzka J, Metman MC, Minami T, Morschhauser A, Mound JE, Nair M, Nakano S, Olsen N, Pavón-Carrasco FJ, Petrov VG, Ropp G, Rother M, Sabaka TJ, Sanchez S, Saturnino D, Schnepf NR, Shen X, Stolle C, Tangborn A, Tøffner-Clausen L, Toh H, Torta JM, Varner J, Vervelidou F, Vigneron P, Wardinski I, Wicht J, Woods A, Yang Y, Zeren Z, Zhou B (2021) International Geomagnetic Reference Field: the thirteenth generation. Earth Planets Space 73(1):49. https://doi.org/10.1186/s40623-020-01288-x

Alken P, Thébault E, Beggan CD, Aubert J, Baerenzung J, Brown WJ, Califf S, Chulliat A, Cox GA, Finlay CC, Fournier A, Gillet N, Hammer MD, Holschneider M, Hulot G, Mand KV, Lesur LPW, Lowes FJ, Macmillan S, Nair M, Olsen N, Ropp G, Rother M, Schnepf NR, Stolle C, Toh H, Vervelidou F, Vigneron P, Wardinski I (2021) Evaluation of candidate models for the 13th generation International Geomagnetic Reference Field. Earth Planets Space 73(1):48. https://doi.org/10.1186/s40623-020-01281-4

Aubert J, Finlay CC (2019) Geomagnetic jerks and rapid hydromagnetic waves focusing at Earth's core surface. Nat Geosci 12(5):393–398. https://doi.org/10.1038/s41561-019-0355-1

Barton CE (1997) International Geomagnetic Reference Field: The seventh generation. J Geomagn Geoelectr 49(2–3):123–148. https://doi.org/10.5636/jgg.49.123

Beggan CD, Kloss A, Amblard PO, Amezza T, Aubert J, Baerenzung J, Brown W, Califf S, Campuano S, Chulliat A, Claveau R, Davies C, Dobrovolsky M, Finlay C, Firsov I, Fournier A, Gailler L, Gillet N, Gomez Perez N, Grayver A, Gwirtz K, Hamoudi M, Holme R, Holschneider M, Jiang Y, Kada M, Korte M, Krasnoperov R, Kuang W, Kudin D, Lauridsen JB, Lemgharbi A, Lesur V, Liu P, Livermore P, Madsen F, Matsushima M, Matzka J, Michaelis I, Minami T, Nair M, Nakano S, Oehler JF, Olsen N, Pavón-Carrasco F, Presnyakov S, Qian B, Rang X, Rogers H, Rother M, Rouxel D, Sabaka T, Sato S, Saynisch-Wagner J, Schanner M, Serrano M, Shakespeare-Rees N, da Silva MV, Soloviev A, Thébault E, Tøffner-Clausen L, Toh H, Wang J, Wardinski I, Watson C, Whaler K, Xiong C, Yan Q, Yang Y, Yao H, Zeren Z, Zhang K, Zhou B (2026) International Geomagnetic Reference Field: the fourteenth generation. Earth Planets Space. https://doi.org/10.1186/s40623-025-02360-0

Beggan CD (2022) Evidence-based uncertainty estimates for the International Geomagnetic Reference Field. Earth Planets Space 74(1):17. https://doi.org/10.1186/s40623-022-01572-y

Beggan C, Kloss C, Smith A, Amblard PO, Amezza T, Aubert J, Baerenzung J, Brown W, Califf S, Campuano S, Chulliat A, Claveau R, Davies C, Dobrovolsky M, Finlay C, Firsov I, Fournier A, Gailler L, Gillet N, Gomez Perez N, Grayver A, Gwirtz K, Hamoudi M, Holme R, Holschneider M, Jiang Y, Kada M, Korte M, Krasnoperov R, Kuang W, Kudin D, Lauridsen JB, Lemgharbi A, Lesur V, Liu P, Livermore P, Madsen F, Matsushima M, Matzka J, Michaelis I, Minami T, Nair M, Nakano S, Oehler JF, Olsen N, Pavón-Carrasco F, Presnyakov S, Qian B, Rang X, Rogers H, Rother M, Rouxel D, Sabaka T, Sato S, Saynisch-Wagner J, Schanner M, Serrano M, Shakespeare-Rees N, da Silva MV, Soloviev A, Thébault E, Tøffner-Clausen L, Toh H, Wang J, Wardinski I, Watson C, Whaler K, Xiong C, Yan Q, Yang Y, Yao H, Zeren Z, Zhang K, Zhou B (2024) IGRF-14 Evaluation. https://doi.org/10.5281/zenodo.14205635

Bishop CM, Nasrabadi NM (2006) Pattern recognition and machine learning, vol 4. Springer

Brown W, Macmillan S, Maume E, Eaton E (2025) A database of geomagnetic observatory monthly means: from historic to the satellite era. Earth Planets Space. https://doi.org/10.1186/s40623-025-02316-4

Chulliat A, Vigneron P, Hulot G (2016) First results from the Swarm Dedicated Ionospheric Field Inversion chain. Earth Planets Space 68(1):104. https://doi.org/10.1186/s40623-016-0481-6

Chulliat A, Nair M, Califf S (2026) Candidate geomagnetic field models for IGRF-14 and secular acceleration since 2020. Earth Planets Space. https://doi.org/10.1186/s40623-025-02362-y

Chulliat A, Brown W, Nair M, Gómez Pérez N, Young LY, Watson C, Boneh N, Beggan C, Meyer B, Paniccia M (2025) The US/UK World Magnetic Model for 2025-2030: Technical report. National Centers for Environmental Information, NOAA. https://doi.org/10.25923/prbc-s316

Chulliat A, Thébault E, Hulot G (2010) Core field acceleration pulse as a common cause of the 2003 and 2007 geomagnetic jerks. Geophys Res Lett. https://doi.org/10.1029/2009GL042019

Claveau R, Gillet N, Amblard PO, Finlay CC (2025) Broadband a priori temporal cross-covariances for the geomagnetic inverse problem: application to

the satellite era. Earth Planets Space 77(1):126. https://doi.org/10.1186/s40623-025-02248-z
Deconinck F, Hulot G, Léger JM, Clausen LB, Pastena M, Lejault JP, Wilkinson J, Caballero DM, Tostado MV, Coïsson P, et al (2025) NanoMagSat status: a 3x16U low-earth orbit constellation to monitor the Earth's magnetic field and the ionospheric environment. In: Small satellites systems and services symposium (4S 2024), SPIE, vol. 13546, pp. 1086–1100. https://doi.org/10.1117/12.3062471
Eymin C, Hulot G (2005) On core surface flows inferred from satellite magnetic data. Phys Earth Planet Inter 152(3):200–220. https://doi.org/10.1016/j.pepi.2005.06.009
Finlay CC, Maus S, Beggan CD, Hamoudi M, Lowes FJ, Olsen N, Thébault E (2010) Evaluation of candidate geomagnetic field models for IGRF-11. Earth Planets Space 62(10):8. https://doi.org/10.5047/eps.2010.11.005
Finlay CC, Kloss C, Olsen N, Hammer MD, Tøffner-Clausen L, Grayver A, Kuvshinov A (2020) The CHAOS-7 geomagnetic field model and observed changes in the South Atlantic Anomaly. Earth Planets Space 72(1):156. https://doi.org/10.1186/s40623-020-01252-9
Firsov I, Kudin D, Soloviev A, Krasnoperov R, Dobrovolsky M (2026) GCRAS candidate field models for IGRF-14. Earth Planets Space. https://doi.org/10.1186/s40623-025-02318-2
Friis-Christensen E, Lühr H, Hulot G (2006) Swarm: A constellation to study the Earth's magnetic field. Earth Planets Space 58(4):351–358
Gillet N, Dall'Asta F, Amblard PO, Claveau R, Aubert J (2024) Waves in Earth's core and geomagnetic field forecast. Phys Earth Planet Inter 357(107):284. https://doi.org/10.1016/j.pepi.2024.107284
Gwirtz K, Sabaka T, Kuang W (2025) A secular variation candidate for IGRF-14 based on core-flow inversion via an ensemble Kalman smoother. Earth Planets Space 77(1):158. https://doi.org/10.1186/s40623-025-02289-4
Huber PJ (1964) Robust estimation of a location parameter. Ann Math Statist 35(73–101):1. https://doi.org/10.1214/aoms/1177703732
Hulot G, Mouël JL, Wahr J (1992) Taking into account truncation problems and geomagnetic model accuracy in assessing computed flows at the core-mantle boundary. Geophys J Int 108(1):224–246. https://doi.org/10.1111/j.1365-246X.1992.tb00852.x
Hulot G, Chauvet L, Deborde R, Léger JM, Jager T, Fillion M, Coïsson P (2026) A DGRF 2020 candidate model only based on Swarm ASM experimental vector mode data improved through a dedicated post-calibration strategy. Earth Planets Space. https://doi.org/10.1186/s40623-025-02343-1
Hulot G, Lhuillier F, Aubert J (2010) Earth's dynamo limit of predictability. Geophys Res Lett. https://doi.org/10.1029/2009GL041869
Hulot G, Vigneron P, Léger JM, Fratter I, Olsen N, Jager T, Bertrand F, Brocco L, Sirol O, Lalanne X, Boness A, Cattin V (2015) Swarm's absolute magnetometer experimental vector mode, an innovative capability for space magnetometry. Geophys Res Lett. https://doi.org/10.1002/2014GL062700
International Association of Geomagnetism and Aeronomy (2024). IGRF-14 coefficients. https://doi.org/10.5281/zenodo.14218973
Kloss C, Finlay CC, Olsen N, Tøffner-Clausen L, Gillet N, Grayver A (2026) The CHAOS-8 geomagnetic field model. Earth Planets Space. https://doi.org/10.1186/s40623-025-02352-0
Langel RA, Hinze WJ (1998) The magnetic field of the Earth's lithosphere: The satellite perspective. Cambridge University Press
Léger JM, Jager T, Bertrand F, Hulot G, Brocco L, Vigneron P, Lalanne X, Chulliat A, Fratter I (2015) In-flight performance of the Absolute Scalar Magnetometer vector mode on board the Swarm satellites. Earth Planets Space. https://doi.org/10.1186/s40623-015-0231-1
Leopardi P (2006) A partition of the unit sphere into regions of equal area and small diameter. Electron Trans Numer Anal 25(12):309–327
Livermore PW, Hollerbach R, Finlay CC (2017) An accelerating high-latitude jet in Earth's core. Nat Geosci 10(1):62–68. https://doi.org/10.1038/ngeo2859
Love JJ, Chulliat A (2013) An INTERnational network of MAGnetic observatories. EOS Trans Am Geophys Union 94(42):373–374
Lowes FJ (1974) Spatial power spectrum of the main geomagnetic field, and extrapolation to the core. Geophys J Int 36(3):717–730. https://doi.org/10.1111/j.1365-246X.1974.tb00622
Lowes FJ (2000) An estimate of the errors of the IGRF/DGRF fields 1945–2000. Earth Planets Space 52(12):1207–1211. https://doi.org/10.1186/BF03352353
Macmillan S, Finlay CC (2011) The International Geomagnetic Reference Field. In: Mandea M, Korte M (eds) Geomagnetic observations and models, vol 5. Springer, pp 265–276
Macmillan S, Maus S, Bondar T, Chambodut A, Golovkov V, Holme R, Langlais B, Lesur V, Lowes F, Lühr H, Mai W, Mandea M, Olsen N, Rother M, Sabaka T, Thomson A, Wardinski I (2003) The 9th-generation international geomagnetic reference field. Geophys J Int 155(3):1051–1056. https://doi.org/10.1111/j.1365-246X.2003.02102.x
Madsen FD, Beggan CD, Brown WJ, Holme R, Lauridsen JB, Whaler KA (2026) IGRF-14 secular variation prediction from core-surface flow acceleration. Earth Planets Space. https://doi.org/10.1186/s40623-025-02347-x
Madsen F, Whaler K, Beggan C, Brown W, Lauridsen J, Holme R (2025) Modelling geomagnetic jerks with core surface flow derived from satellite gradient tensor elements of secular variation. Phys Earth Planet Inter. https://doi.org/10.1016/j.pepi.2025.107336
Mauersberger P (1956) Das mittel der energiedichte des geomagnetischen hauptfeldes an der erdoberflache und seine saulare anderung. Gerlands Beitr Geophys 65:207–215
Metman MC, Livermore PW, Mound JE, Beggan CD (2019) Modelling decadal secular variation with only magnetic diffusion. Geophys J Int 219:S58–S82. https://doi.org/10.1093/gji/ggz089
Olsen N (2002) A model of the geomagnetic field and its secular variation for epoch 2000 estimated from ørsted data. Geophys J Int 149(2):454–462. https://doi.org/10.1046/j.1365-246X.2002.01657.x
Qian B, Xiong C, Wang F, Yang Y, Rang X, Huang Y (2025) WHUEMM: Global core field modelling from multiple satellites and comparative evaluation of inversion strategy. Earth Planets Space 77(1):183. https://doi.org/10.1186/s40623-025-02313-7
Ramsay JO, Silverman BW (2005) Functional data analysis, 2nd edn. Springer
Rogers H, Mandea M (2026) How do core surface flow models vary when inverted from IGRF-14 candidate field models? Earth Planets Space. https://doi.org/10.1186/s40623-025-02307-5
Rother M, Schanner M, Korte M, Michaelis I, Matzka J, da Silva MVS (2026) The GFZ IGRF candidate models and an assessment of secular variation predictions. Earth Planets Space. https://doi.org/10.1186/s40623-026-02426-7
Sato S, Nakano S, Lesur V, Matsushima M, Minami T, Toh H (2026) Recurrent neural network trained with the extended Kalman filter to forecast the geomagnetic secular variation for IGRF-14. Earth Planets Space. https://doi.org/10.1186/s40623-025-02338-y
Serrano M, Pavón-Carrasco F, Campuzano S, Marsal S, Torta J, Tordesillas JM, Fiz J (2026) The Spanish contribution to IGRF-14. Earth Planets Space. https://doi.org/10.1186/s40623-026-02368-0
Shakespeare-Rees N, Livermore P, Davies C, Rogers H, Beggan C, Brown W, Finlay C (2026) Forecasting secular variation using physics-informed neural networks. Earth Planets Space. https://doi.org/10.1186/s40623-026-02427-6
Shen X, Zhang X, Yuan S, Wang L, Cao J, Huang J, Zhu X, Piergiorgio P, Dai J (2018) The state-of-the-art of the China Seismo-Electromagnetic Satellite mission. Sci China Technol Sci 61(5):634–642. https://doi.org/10.1007/s11431-018-9242-0
Smith ARA, Pačes M, Swarm DISCs (2022) Python tools for ESA's Swarm mission: VirES for Swarm and surrounding ecosystem. Front Astronom Space Sci. https://doi.org/10.3389/fspas.2022.1002697
Thébault E, Finlay CC, Alken P, Beggan CD, Canet E, Chulliat A, Langlais B, Lesur V, Lowes FJ, Manoj C, Rother M, Schachtschneider R (2015) Evaluation of candidate geomagnetic field models for IGRF-12. Earth Planets Space 67:112. https://doi.org/10.1186/s40623-015-0273-4
Wardinski I, Terra-Nova F, Amit H (2026) Models and predictions of Earth's magnetic field based on geomagnetic observatory data. Earth Planets Space. https://doi.org/10.1186/s40623-026-02410-1
Winch DE, Ivers DJ, Turner JPR, Stening RJ (2005) Geomagnetism and Schmidt quasi-normalization. Geophys J Int 160(2):487–504. https://doi.org/10.1111/j.1365-246X.2004.02472.x
Yang Y, Zeren Z, Hulot G, Wang J, Olsen N, Yang S, Zhou B, Magnes W, Cheng B, Huang J, Chauvet L, Yang D, Lammegger R, Lin J, Liu D, Lu H, Zhou N, Yan R, Zhang Z, Chu W, Xu S, Huang H, Cui J, Tan Q, Li W, Guo F (2026) Second Generation of CSES Global Geomagnetic Field Model (CGGM-2) and associated candidate models for IGRF-14. Earth Planets Space. https://doi.org/10.1186/s40623-025-02361-z

Yao H, Liu P, Yan Q, Jiang Y, Xu J, Yin L, Ren Z, Lin Y, Feng Y, Pan Y, Zhang K (2025) MISTA candidate magnetic field models for IGRF-14 derived from MSS-1, Swarm and observatory data. Earth Planets Space 77(1):184. https://doi.org/10.1186/s40623-025-02304-8

Zhang K (2023) A novel geomagnetic satellite constellation: Science and applications. Earth Planet Phys 7(1): 4–21. https://doi.org/10.26464/epp2023019

Publisher's Note